Relevance of fermion loops for W^+W^- scattering at the LHC

Carlos Quezada-Calonge,[*] Antonio Dobado,[†] and Juan José Sanz-Cillero[‡]
Departamento de Física Teórica and IPARCOS, Facultad de Ciencias Físicas, Universidad Complutense de Madrid, 28040 Madrid, Spain

(Received 26 November 2022; accepted 28 March 2023; published 18 May 2023)

We study the one-loop corrections to W^+W^- elastic scattering within the framework of effective theories. Rescattering via intermediate electroweak would-be-Goldstone bosons dominate at high energies, as the corresponding loop diagrams with these intermediate bosons scale like $\mathcal{O}(s^2/v^4)$ in the chiral effective counting. In the present article, we focus our attention on the usually neglected fermion-loop corrections which scale like $\mathcal{O}(M_{\rm fer}^2 s/v^4)$ in the Higgs effective field theory (HEFT). Although this dependency is formally suppressed for $s \to \infty$ with respect to the ones from boson loops, the large top mass can lead to a numerical competition between fermion and boson loops at intermediate energies of the order of a few TeV. The central goal of the present study is to assess the importance of these fermion loops. For this, since the fermion contribution scales with the mass of the fermions, we have calculated the imaginary part induced by loops of the heaviest fermions, top and bottom quarks, in $W^+W^- \to W^+W^-$ elastic scattering and compared them with the loop contributions from purely bosonic loops, as a large imaginary part would be a clear indicator of large fermion-loop effects. We have examined the dependence of both amplitudes on the effective couplings, allowing an $\mathcal{O}(10\%)$ deviation from the Standard Model. In some cases, boson loops dominate over top and bottom corrections, as expected. However, we find that there are regions in the space of effective parameters that yield a significant—and even dominant—imaginary contribution from fermion loops. In addition to our conclusions for the general HEFT, we also provide analyses particularized to some benchmark points in the $SO(5)/SO(4)$ minimal composite Higgs model.

DOI: 10.1103/PhysRevD.107.093006

I. INTRODUCTION

The discovery of the Higgs boson in 2012 by CMS and ATLAS [1,2] has provided the last missing piece of the Standard Model (SM). Over the past decade, in the absence of new direct signals which may suggest new physics (NP), much effort has been put into high-precision tests of the SM through LHC data. The hope is that by observing small deviations we may be able to elucidate the underlying NP at higher energies. Within this context, one of the main processes for this exploration is vector boson scattering (VBS). Deviations from the SM arising from a strongly interacting electroweak symmetry breaking sector [3] are expected to enhance the scattering of the longitudinal components of W and Z bosons at high energies. In the absence of new states, the most general description of the NP is the so-called Higgs effective field theory (HEFT), which is a sort of Higgs-equipped electroweak chiral Lagrangian (EChL) [4,5]. For VBS at a center-of-mass (c.m.) energy well over the WW threshold ($\sqrt{s} \gg M_W$), an important tool is the equivalence theorem (ET) [6]. This relates, up to $\mathcal{O}(M_W/\sqrt{s})$ corrections, processes with longitudinal electroweak (EW) gauge bosons $W^\pm$ and Z and amplitudes with EW would-be-Goldstone bosons (WBGBs) ω^a. By neglecting these $\mathcal{O}(M_W/\sqrt{s})$ contributions, the so-called naive equivalence theorem (NET), the calculation of the amplitudes gets highly simplified. For instance, in the case of this article, the more involved $W_L^+W_L^- \to W_L^+W_L^-$ computation would be traded for the simpler $\omega^+\omega^- \to \omega^+\omega^-$ calculation. Notice that in the NET we have replaced the external longitudinal gauge bosons with WBGBs, but all particles (gauge bosons and WBGBs) must be considered in the internal lines. However, WBGBs interact through derivative operators and formally dominate at high energies in strongly interacting models. For this reason, it often works in this framework to consider only WBGB loops as a sensible first approach to the

[*]cquezada@ucm.es
[†]dobado@fis.ucm.es
[‡]jjsanzcillero@ucm.es

problem [7].[1] Nevertheless, new studies [8] begin to include the physical gauge bosons as internal lines, hence using the ET as originally formulated.

In the HEFT, leading-order (LO) contributions to the amplitude appear at tree level and scale like $\mathcal{O}(p^2/v^2) \sim \mathcal{O}(s/v^2)$. At next-to-leading order (NLO) in the HEFT's chiral expansion, the amplitudes get $\mathcal{O}(p^4/v^4)$ corrections, with p representing soft scales of the low-energy effective theory (masses, c.m. energy, etc.). More precisely, WBGB loops are NLO in the chiral expansion and scale like $\mathcal{O}(s^2/v^4)$, whereas fermion loops show an $\mathcal{O}(M_{\text{fer}}^2 s/v^4)$ dependence. Hence, the latter are usually neglected: WBGB loops will produce stronger deviations from the SM as we increase the center-of-mass energy.

In the present article, we provide a systematical quantitative study of the importance of these fermion-loop contributions to the W^+W^- scattering at the energies relevant at the LHC within the context of the HEFT. During this analysis, we have realized that in some cases an accurate calculation of the boson loops requires going beyond the NET. At high energies, HEFT models with Higgs couplings very close to the SM ones have boson-loop contributions which are identically zero in the zero mass limit, $M_{W,Z,h,\text{fer}} \to 0$. Hence, in this situation, the deviations from the SM enter in numerical competition with the corrections to the NET. For this reason, in this article, we go beyond the NET and perform the analysis of W^+W^- scattering rather than $\omega^+\omega^-$. Some preliminary results in the NET were provided in Ref. [9].

It is well known that fermion loops are proportional to the masses of the particles in the EW fermion doublet inside the loop and to their Higgs effective couplings. Experimentally, Higgs-fermion couplings are still allowed for deviations within a $\pm\mathcal{O}(10\%)$ with respect to the SM values or larger [10]. We will focus on the heaviest xquark doublet, given by the (t, b) quarks, but results can be extended to the remaining Standard Model EW doublets in a straightforward way. Nevertheless, they will be numerically negligible, because their masses are much smaller than the Higgs vacuum expectation value ($M_{\text{fer}} \ll v \approx 246$ GeV).

In this work, we will focus on the imaginary part of fermionic and boson-loop contributions to WW scattering. This choice is twofold:

(1) Since the imaginary part first appears in the scattering amplitude at NLO in the low-energy chiral counting, it is not masked by the purely real LO amplitude or the real tree-level corrections at NLO, determined by additional counterterms. This allows us to compute the imaginary part of all the absorptive one-loop Feynman diagrams that contribute to this process without needing renormalization, as they are finite at this order. The real contributions that do need renormalization are subject of a future work [11].

(2) There is an absence of available studies where mass effects are taken into account for boson-loop corrections. Among the literature in the HEFT, studies can be found focusing on contributions to electroweak Goldstone boson scattering via the use of the naive (or not) equivalence theorem [3,7,12]. In this context, it is common to neglect the effects of the masses of these bosons in order to make calculations easier. Since in our case it is critical to maintain the mass of the top (at least) and bottom quark, the comparison between the fermionic and bosonic loops (treated as massless) could be misleading when our intention is precisely to gauge those mass effects. A detailed study of the real part of fermionic loops to WW scattering would also need, in principle, a complete study of the bosonic loop corrections to WW scattering (not GB) without neglecting the masses of the bosons and without using a version of the equivalence theorem. For some recent WZ scattering studies on these aspects, we refer to Ref. [13].

The quantity of interest in this article will be the ratio of fermion- and boson-loop contributions to the imaginary part of the scattering amplitude. More specifically, we will study the first two partial-wave amplitudes (PWAs), $J = 0$ and $J = 1$. For this, we will make use of perturbative unitarity which connects the imaginary part of an intermediate *two-particle-loop* contribution with the amplitude of tree-level processes with the same two particles as a final state. The calculation and study of the real parts of these one-loop amplitudes will be provided elsewhere [11]. Nevertheless, it is reasonable to assume that if the imaginary part of fermion loops is large, one may also have sizable contributions in their real part.

The custodial limit (sometimes called isospin limit) also provides a convenient approximation to our calculation. By neglecting explicit custodial breaking terms in the HEFT Lagrangian, expressions are simplified and calculations become, in general, simpler. However, we have two sources of custodial symmetry breaking. In the first place, the components of the EW fermion doublets have very different masses ($M_t \neq M_b$). In addition, $g' \neq 0$ introduces a small custodial symmetry violation which leads, e.g., to the EW gauge boson mass difference ($M_W \neq M_Z$). In this article, we will always consider the physical top and bottom masses, while the custodial breaking due to the $U(1)_Y$ coupling will be neglected in a first approximation to the problem [$(M_Z^2 - M_W^2) \ll M_W^2$]. This $g' = 0$ limit makes the analysis simpler and clearer, as the number of intermediate channels is much smaller (photons decouple when $g' \to 0$).

[1]It is important to note that the full—generalized—equivalence theorem also provides the subdominant corrections [6] and an exact relation can be established at the price, nonetheless, of making the computation more involved.

However, we will later complement this computation with the full calculation for $g' \neq 0$, finding similar results.

In this article, we have concluded previous preliminary studies [9,14] by including all possible two-particle intermediate physical states for the elastic W^+W^- scattering, including all possible intermediate gauge boson polarizations, and with $M_t \neq M_b$ and $g' \neq 0$. Thus, the available two-particle absorptive cuts are $t\bar{t}$ and $b\bar{b}$ in the case of fermionic cuts and W^+W^-, ZZ, hh, Zh, $\gamma\gamma$, γZ, and γh for bosonic intermediate states.

The article is organized as follows. In Sec. II, we introduce the HEFT Lagrangian discussing the problems that arise when one uses the equivalence theorem and the decision to go beyond it. In Sec. III, we show how the imaginary part of the corrections of both boson and fermion loops to the partial-wave amplitudes of W^+W^- scattering are calculated via the optic theorem and design the quantity of interest R_J ($J = 0, 1$) that will reveal the importance of fermion-loop corrections. In Sec. IV, we take the often used $g' = 0$ limit to calculate R_J and observe the significance of fermions in some regions of the parameter space of the HEFT couplings. Section V goes beyond the $g' = 0$ limit to capture the effects of intermediate exchanges that were neglected in the previous section. In Sec. VI, we use the predictions from the minimal composite Higgs model as inputs for the HEFT couplings and address the relevance of the fermion corrections in this model. Finally, in Sec. VII, we provide some conclusions. Technical details on kinematics, partial waves, and some lengthier expressions for the scattering amplitudes are relegated to the Appendixes.

II. HEFT LAGRANGIAN

In this section, we present the relevant EW chiral Lagrangian for the elastic WW scattering analysis discussed in this article. However, in a first approximation, we approached the study by making use of the NET, where the longitudinal gauge bosons in the external legs of the amplitude are replaced by EW Goldstone bosons, which is accurate up to $M_{W,Z}/\sqrt{s}$ corrections. Though not stated in the theorem, it is also common in the literature to ignore gauge boson intermediate exchanges in this ET approximation, considering only scalar exchanges (Goldstone boson interactions carry additional derivatives in their interaction with respect to the gauge boson ones). Thus, individual scattering diagrams with Goldstone vertices grow like E^2, eventually violating the unitarity bound. Nevertheless, in the exact SM limit, there is a fine cancellation between the various contributions to the total amplitude, which behaves like E^0; the unitarity bound is always preserved, and the theory is renormalizable. In that SM limit, the contribution of the intermediate gauge boson exchanges is crucial. Hence, in beyond-SM (BSM) scenarios that are nonetheless close to the SM, these contributions cannot be ignored. Moreover, for energies below the TeV, near the WW production threshold, the corrections to the NET eventually become important. For these two reasons, we have also performed the present analysis beyond the NET limit: In addition to the $\omega^+\omega^-$ scattering in the NET, we have also computed the actual $W_L^+W_L^-$ longitudinal gauge boson scattering. Although we will focus on the latter, we will briefly discuss the difference in the following subsection.

A. Effective Lagrangian in the equivalence theorem limit

In this first approach, we will just consider in our EFT description the scalar bosons and the fermions we are interested in. Since the fermion contributions will be proportional to the masses of the fermions in the weak doublets, we will include only the top and bottom quarks in the effective Lagrangian below. The remaining fermions nonetheless can also be incorporated into the theory in a straightforward way, if required.

At LO, $\mathcal{O}(p^2)$, the relevant part of our effective Lagrangian is given by [4,5,15–19]

$$\mathcal{L}_2 = \mathcal{L}_S + \mathcal{L}_{\text{kin-F}} + \mathcal{L}_{\text{Yuk}}, \tag{1}$$

where

$$\mathcal{L}_S = \frac{v^4}{4}\mathcal{F}(h)\text{Tr}\{\partial_\mu U^\dagger \partial^\mu U\} + \frac{1}{2}\partial_\mu h \partial^\mu h - V(h), \tag{2}$$

$$\mathcal{L}_{\text{kin-F}} = i\bar{t}\not{\partial}t + i\bar{b}\not{\partial}b, \tag{3}$$

$$\mathcal{L}_{\text{Yuk}} = -\mathcal{G}(h)\left[\sqrt{1-\frac{\omega^2}{v^2}}(M_t\bar{t}t + M_b\bar{b}b) + i\frac{\omega^0}{v}(M_t\bar{t}\gamma^5 t - M_b\bar{b}\gamma^5 b)\right.$$
$$\left. + i\frac{\sqrt{2}\omega^+}{v}(M_b\bar{t}P_R b - M_t\bar{t}P_L b) + i\frac{\sqrt{2}\omega^-}{v}(M_t\bar{b}P_R t - M_b\bar{b}P_L t)\right], \tag{4}$$

with $\mathcal{L}_{\rm Yuk}$ providing the Yukawa interactions between fermions and scalars[2] [h is the Higgs and ω^a the WBGB fields with $\omega^2=\sum_j(\omega_j)^2$], $P_{R,L}=\frac{1}{2}(1\pm\gamma_5)$ are the chirality projectors, and $v\simeq 246$ GeV. For the Goldstones in Eq. (2), we are using in this article the coset representation $U=\sqrt{1-\omega^2/v^2}+i\omega^a\sigma^a/v$ [20]. In front of these operators, symmetry invariance allows us to insert a general function of the Higgs field singlet h with an analytical expansion of the form

$$\mathcal{G}(h)=1+c_1\frac{h}{v}+\cdots,\quad \mathcal{F}(h)=1+2a\frac{h}{v}+b\frac{h^2}{v^2}+\cdots,\quad \text{and}$$
$$V(h)=\frac{M_h^2}{2}h^2+d_3\frac{M_h^2}{2v}h^3+d_4\frac{M_h^2}{8v^2}h^3+\cdots. \tag{5}$$

In the SM case, one has $a=b=c_1=d_3=d_4=1$ and zero for any higher powers of h. These couplings (a,b,c_1,d_3) are the only relevant parameters in $\mathcal{F}(h)$, $\mathcal{G}(h)$, and $V(h)$ for the present W^+W^- elastic scattering study.

As was mentioned in the introduction, we first computed the boson-loop contributions to WW scattering in the context of the NET in the Landau gauge, neglecting diagrams with gauge bosons in the intermediate internal lines. For strongly interacting BSM scenarios with $a\neq 1$, these NET-simplified calculations do reproduce well the behavior of W_LW_L scattering. However, in the SM case, the NET does not recover the right prediction for $W_LW_L\to W_LW_L$ scattering if intermediate gauge boson exchanges are not taken into account and the $\omega\omega\to\omega\omega$ scattering fails to yield the precise prediction in this important case. Hence, we move beyond the NET and compute the loop contributions, including physical gauge bosons in the tree-level calculation of this amplitude. This full tree-level amplitude $W_LW_L\to W_LW_L$ has already been used for the $g'=0$ case in Ref. [9].

Regarding the fermion contribution via the tree-level scattering $\mathcal{A}(W_L^+W_L^-\to f\bar{f})$, we have first reproduced via the NET and HEFT (in the Landau gauge) the results in Ref. [21] for $\omega^+\omega^-\to f\bar{f}$.[3] Nonetheless, we find that the NET shows further complications in this case. The SM amplitude with same-sign fermion helicities $(++,--)$ does not match its NET counterpart $\mathcal{A}(\omega^+\omega^-\to f\bar{f})$ at high energies. In the limit when $M_W/\sqrt{s}\to 0$, at fixed s and M_t, we find that this amplitude coincides with the corresponding WBGB scattering. However, this is different to the high-energy limit $s\to\infty$, at fixed M_W and M_t, where we have found an important discrepancy when the HEFT is not used in the Feynman gauge between both amplitudes in the SM case. This difference can be observed directly in the first partial-wave amplitude $a_{J=0}$. For completion, we turned to the SMEFT and calculated $\mathcal{A}(W_L^+W_L^-\to f\bar{f})$ to find that also in the SMEFT this amplitude fails to reproduce the scattering with physical bosons. To illustrate, Fig. 1 shows the SM $J=0$ PWAs for $W_L^+W_L^-\to t\bar{t}$ and $\omega^+\omega^-\to t\bar{t}$ for the Feynman gauge in the SMEFT, where one can see that the difference is significant even at high energies (of the order of 70%). Fortunately, it is possible to recover the full $W_L^+W_L^-\to f\bar{f}$ amplitude if, instead of applying the NET, one employs the full generalized ET [6,20]. Similar concerns about the NET were raised in previous works when dealing with WBGB amplitudes, effective Lagrangians, and possible heavy scalars [22–24]. The discussion of this topic is beyond the scope of this article, and it is relegated to a future work [11].

It is important to remark that this high-energy discrepancy occurs in the SM only due to a fine cancellation. For BSM theories with $ac_1\neq 1$, the NET works well and the WBGB scattering amplitudes reproduce the longitudinal gauge boson scatterings at high energies. For instance, we find that in BSM scenarios $\mathcal{A}(W_L^+W_L^-\to t\bar{t})\approx(-1)\times\mathcal{A}(\omega^+\omega^-\to t\bar{t})\sim\sqrt{N_C}(1-ac_1)\sqrt{s}M_t/v^2$ for $s\gg M_W^2,M_t^2$. However, the latter leading term is canceled in the SM. The first nonvanishing contributions for both amplitudes differ at high energies by a term $\propto\sqrt{N_c}\frac{M_tM_W^2}{\sqrt{s}v^2}$. Although this term might not look important at high energies, it becomes crucial in the SM limit $a=c_1=1$ when the formally dominant $\mathcal{O}(m_t\sqrt{s})$ terms vanish both $W_L^+W_L^+$ and WBGB amplitudes. The comparison of these two amplitudes can be seen in Fig. 1.

In summary, given all these considerations, we will always be working with the actual $W_L^+W_L^-$ scattering amplitudes, for both bosonic and fermionic intermediate absorptive cuts.

B. Effective Lagrangian beyond the equivalence theorem limit

Ultimately, for a study beyond the ET, one must also add the EW gauge boson interactions to the EChL [4]. Thus, the relevant part of the LO, $\mathcal{O}(p^2)$, Lagrangian for the WW study in this article is given by [4,5,15–19]

$$\mathcal{L}_2=\mathcal{L}_S+\mathcal{L}_{\rm Yuk}+\mathcal{L}_{\text{kin-F}}+\mathcal{L}_{\rm YM}, \tag{6}$$

with

$$\mathcal{L}_S=\frac{v^4}{4}\mathcal{F}(h)\mathrm{Tr}\{(D_\mu U)^\dagger D^\mu U\}+\frac{1}{2}\partial_\mu h\partial^\mu h-V(h), \tag{7}$$

[2]The Yukawa Lagrangian provided in Eq. (4) is indeed the general chiral expression of the Yukawa interaction $\mathcal{L}_{\rm Yuk}=-\mathcal{G}(h)\bar{Q}_LUM_QQ_R+\text{H.c.}$ expressed in the spherical coordinate coset representation $U=\sqrt{1-\omega^2/v^2}+i\omega^a\sigma^a/v$ that we will be using throughout the article, with $Q^T=(t,b)$ and $M_Q=\mathrm{diag}(M_t,M_b)$.

[3]Notice that the $\omega^+\omega^-\to f\bar{f}$ amplitude in Ref. [21] does not include gauge bosons in the internal lines. We have also removed these contributions in our calculation for the comparison with this work.

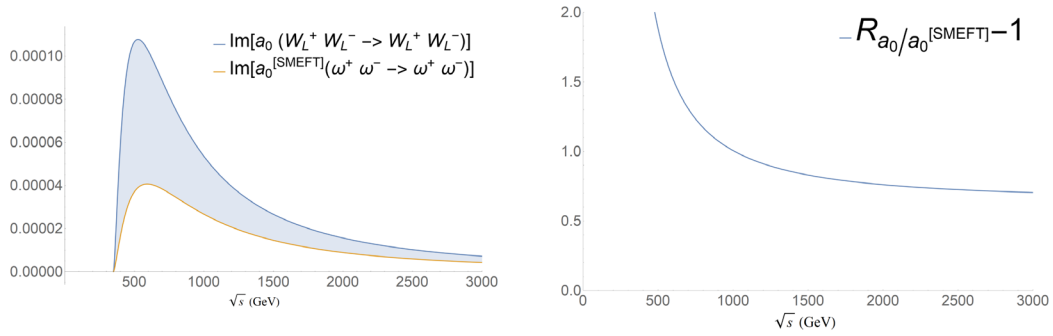

FIG. 1. Left: imaginary part of the SM top-quark one-loop diagram in the $a_{J=0}$ partial-wave amplitude [coming from tree-level $\mathcal{A}(W_L^+W_L^- \to t\bar{t})$] and its equivalence theorem analog partial wave $a_{J=0}^{[\mathrm{SMEFT}]}$ [given by tree-level $\mathcal{A}(\omega^+\omega^- \to t\bar{t})$ in the SMEFT for the Feynman–'t Hooft gauge]. Right: ratio $R_0 = \mathrm{Im}[a_0]/\mathrm{Im}[a_0^{[\mathrm{SMEFT}]}]$ of these same partial-wave amplitudes.

$$\mathcal{L}_{\text{kin-F}} = i\bar{t}\not{D}t + i\bar{b}\not{D}b, \tag{8}$$

where the covariant derivatives in $\mathcal{L}_{\text{kin-F}}$ and $\mathcal{L}_S$ now contain the couplings with the EW gauge bosons, $\mathcal{L}_{\text{YM}}$ is the standard $SU(2)_L \times U(1)_Y$ Yang-Mills Lagrangian, and $\mathcal{L}_{\text{Yuk}}$ is the previous Yukawa Lagrangian in Eq. (4).

III. LOOP CORRECTIONS TO ELASTIC $W_L^+W_L^-$ SCATTERING

Starting from this Lagrangian, we have computed the fermion-loop contribution to the elastic $W_L^+W_L^-$ scattering amplitude for the (t, b) quark doublet. At LO in the chiral expansion, $\mathcal{O}(p^2)$, the amplitude $\mathcal{A}_2$ is purely real, and it is given by tree-level diagrams made from $\mathcal{L}_2$ vertices. Its first correction, $\mathcal{A}_4$, shows up at $\mathcal{O}(p^4)$ in the chiral counting. It acquires a real tree-level contribution $\mathcal{A}_{4,\text{tree}}$ from the corresponding effective couplings in the NLO Lagrangian $\mathcal{L}_4$ (namely, a_4 and a_5). Likewise, one-loop diagrams made of $\mathcal{L}_2$ vertices also yield a $\mathcal{A}_{4,1\ell}$ contribution to the $\mathcal{O}(p^4)$ amplitude and provide the first contribution to the imaginary part of the amplitude $\mathcal{A}$.

Up to the order studied in this work, $\mathcal{O}(p^4)$, the real part of the amplitude is provided by the aforementioned three contributions, $\mathrm{Re}\mathcal{A} = \mathcal{A}_2 + \mathcal{A}_{4\text{tree}} + \mathrm{Re}\mathcal{A}_{4,1\ell}$. This makes the study of the NLO one-loop corrections cumbersome. On the other hand, the imaginary part receives contributions only from one-loop diagrams up to this order, $\mathrm{Im}\mathcal{A} = \mathrm{Im}\mathcal{A}_{4,1\ell}$. This makes the study of the importance of fermion corrections much simpler and clearer, and it will be the procedure followed in this article. More specifically, we will be studying the imaginary part of the helicity amplitudes introduced in Ref. [25]. For the particular case of particles with helicity $\lambda = 0$, the Wigner rotation matrices reduce to the well-known Legendre polynomials. This allows us to write the amplitude as a sum of the projected PWAs $a_J(s)$:

$$\mathcal{A}(s,t) = \sum_J 16\pi K(2J+1)P_J(\cos\theta)a_J(s), \tag{9}$$

with $K = 1$ ($K = 2$) for distinguishable (indistinguishable) final particles. In the physical energy region, $\mathrm{Im}a_J(s)$ will be provided by the one-loop absorptive cuts in the s channel, which we will use to label the various contributions.

In scattering amplitudes with only bosons in the external legs, it is possible to clearly separate fermion and boson loops. We will measure the relevance of each of these two contributions. For this, we will use the following notation to refer to the corresponding absorptive cuts:

$$\begin{aligned} \mathrm{fer}_J &= \mathrm{Im}a_J|_{b\bar{b},t\bar{t}}, \\ \mathrm{bos}_J &= \mathrm{Im}a_J|_{\gamma\gamma,\gamma Z,\gamma h,W^+W^-,ZZ,Zh,hh}. \end{aligned} \tag{10}$$

Notice that the channels are arranged by increasing mass, as they will be presented later in the figures. The absorptive cuts with intermediate longitudinal vector bosons WW, ZZ, and hh can be found in Refs. [22,26,27], respectively. The rest are provided in the Appendixes. In this work, we have included the contribution from not only intermediate longitudinal modes but also the transverse ones. Beyond the NET approximation, there are also contributions from the intermediate channels Zh that we did not include in a previous work [9,14].

However, in the massless limit, all the mentioned one-loop corrections contain forward ($\cos\theta = 1$) and/or backward ($\cos\theta = -1$) divergences. In bos_J, these singularities arise in the limit $M_W, M_Z \to 0$ due to the exchange of W, Z, and γ gauge bosons in crossed channels (as the photon is massless, one always finds a forward divergence for the W^+W^- intermediate cut). On the other hand, the amplitudes with intermediate $t\bar{t}$ and $b\bar{b}$ absorptive cuts have a forward divergence for $M_b \to 0$ and $M_t \to 0$, respectively. One can also identify a distinctive pattern for this large forward or backward contribution to the different partial waves: The singular behavior of the ZZ, hh, $\gamma\gamma$, and γh

channels is relevant only for even J; the forward and backward divergences of the Zh and γZ cuts arise just for odd J; finally, since in the massless limit the $t\bar{t}$, $b\bar{b}$, and W^+W^- channels have only forward divergences, they are relevant for both even and odd J PWAs.

In general, the nonzero mass of weak gauge bosons and fermions regulates the indicated divergences, except for one present in the W^+W^- absorptive cut. For the latter, we encounter a divergent diagram arising from the exchange of a photon in the t channel, making its PWA projection integral divergent at $\cos\theta \to 1$. To confront this issue, we will consider two strategies.

(1) *Assume $g' = 0$ and integrate over the whole solid angle.*—In this scenario, $M_Z = M_W$ and thus, the photon decouples ($e = g' \cos\theta_W = 0$), because the W^+W^- cut forward photon divergence is absent. In addition, the $\gamma\gamma$, γZ, and γh channels vanish, simplifying the analysis. In this case, we can perform the complete angular integration and project onto PWAs. This would correspond to the custodial limit but for the fact that we keep $M_t \neq M_b$.

(2) *Impose angular cuts.*—In order to deal with the divergence from the W^+W^- channel, we perform the PWA integration within the angular limits $|\cos\theta| \leq (\cos\theta)_{\max}$ for the intermediate particles (with, e.g., $\cos\theta_{\max} = 0.9$). This approach allows us to go beyond the $g' = 0$ limit, incorporating all the aforementioned cuts in Eq. (10). We will refer to these amplitudes $\tilde{a}_J(s)$ as pseudo-PWAs (p-PWAs). Although the p-PWAs are now finite and well defined (even in the massless limit), we note that they lose many of the interesting PWA properties: The clear separation of the different angular momenta no longer holds, and analogous PWA unitarity relations fail. Nevertheless, these p-PWAs allow us to include other channels and obtain qualitatively results beyond the $g' = 0$ limit. Other approaches, like, e.g., including by hand an artificial mass for the photon, were considered, but this irremediably spoils gauge invariance and the high-energy behavior. Because of this, imposing an angular cut to the physical gauge-invariant amplitude is a more attractive idea. In addition, experimental results are often restricted to a fixed angular range given by the configuration of the detectors.

Moving on, it is important to note which particular couplings enter in each PWA:

$$\begin{aligned} &J = 0\text{: } \mathrm{fer}_0 \to a, c_1, \\ &\mathrm{bos}_0 \to a, b, d_3, \\ &J = 1\text{: } \mathrm{fer}_1 \to \text{no dependence on } a, b, c_1 = \mathrm{SM}, \\ &\mathrm{bos}_1 \to a. \end{aligned} \tag{11}$$

The main goal of the present work is to point out that there are regions of the parameter phase space where fermion loops become as important as the bosonic ones and should not be neglected. To this goal, we introduce the ratio

$$R_J = \frac{\mathrm{fer}_J}{\mathrm{bos}_J + \mathrm{fer}_J}. \tag{12}$$

Values of R_J close to zero will indicate that we can safely drop fermion loops, while deviations from this value will point out the relevance of fermions in WW scattering. Although it is commonly assumed that fermion loops are negligible in most of the parameter space, we will see that this is not true for some particular channels and in some regions of the effective couplings.

In the following, we will focus on the contributions from fermion loops to the first two partial waves $J = 0$, 1. In order to do this, we will use perturbative unitarity which connects the imaginary part of an intermediate two-particle-loop contribution with the amplitude of tree-level processes with the same two particles as a final state. This allows us to write all possible diagrams that contribute to the imaginary part of the amplitude, and, since the imaginary contributions are finite, they do not require renormalization. For more details the reader can consult Appendix A.

By using perturbative unitarity, we can write down the fermionic contribution to the one-loop imaginary part of the partial waves in terms of the tree-level amplitudes $\mathcal{A}(W^+W^- \to F\bar{F}) \equiv Q^{\Delta\lambda,F}$ (one for the production of each intermediate fermion state $F\bar{F}$), with $Q^{0,F} = \frac{1}{\sqrt{2}}(Q^{++,F} - Q^{--,F}) = \sqrt{2}Q^{++,F}$, $Q^{+-,F}$, and $Q^{-+,F}$. For $J = 0$ only the $Q^{0,F}$ combination is necessary for the partial-wave projection $Q_J^{\Delta\lambda,F}$, while for $J = 1$ three ($Q^{0,F}$, $Q^{+-,F}$, $Q^{-+,F}$) enter in the projection:

$$\mathrm{fer}_0 = \mathrm{Im}a_0(s)|_{t\bar{t},b\bar{b}} = \sum_{F=t,b} \beta_F |Q_0^{0,F}|^2 \theta(s - 4M_F^2), \tag{13}$$

$$\begin{aligned} \mathrm{fer}_1 &= \mathrm{Im}a_1(s)|_{t\bar{t},b\bar{b}} \\ &= \sum_{F=t,b} \beta_F \left(|Q_1^{0,F}|^2 + |Q_1^{+-,F}|^2 + |Q_1^{-+,F}|^2 \right) \theta(s - 4M_F^2), \end{aligned} \tag{14}$$

where $\beta_F = \sqrt{1 - 4M_F^2/s}$ and the partial-wave projections are defined as [7]

$$Q_J^{\Delta\lambda} = \frac{1}{64\pi^2 K} \sqrt{\frac{4\pi}{2J+1}} \int Q^{\Delta\lambda}(s,\Omega) Y^*_{J,\Delta\lambda}(\Omega) d\Omega, \tag{15}$$

where $Y_{JM}(\Omega)$ are the spherical harmonics and $\Delta\lambda$ is the helicity difference $\Delta\lambda = \lambda_1 - \lambda_2$, with the superindex F omitted for simplicity.

Additionally, we can also calculate the relative cumulative PWA, which we will denote as

$$\chi_i^J = \frac{\sum_{n=1}^{i} \mathrm{Im}a_j|_n}{\mathrm{Im}a_J},$$

where $\mathrm{N_{ch}}$ is the total number of absorptive channels, $\mathrm{Im}a_J = \sum_{n=1}^{\mathrm{N_{ch}}} \mathrm{Im}a_J|_n$ is the total imaginary part of the a_J PWA, and $\mathrm{Im}a_J|_n$ represents the absorptive contribution from channel n—either bosonic or fermionic—which are arranged in increasing order of their mass threshold. The analytical expression of the tree-level amplitudes that provide the imaginary part of the one-loop diagrams is rather lengthy and has been relegated to Appendix C. All calculations have been performed within arbitrary renormalizable R_ξ gauges with parameters ξ_W, ξ_Z, and ξ_A. We have checked that the full amplitudes are gauge independent, as expected.

IV. IMPORTANCE OF FERMION LOOPS IN THE $g' = 0$ LIMIT

We will start our phenomenological study by considering the $g' = 0$ limit. In the absence of fermion masses, this implies that custodial symmetry is preserved. Actually, fermion masses are not the problem but rather the mass splitting of the fermion multiplets: Custodial symmetry is restored in the limit $g' = 0$ and $M_t = M_b$ (and similarly for each quark and lepton doublet). This approximate custodial or isospin symmetry is very useful to simplify and classify the contribution from bosonic channels, as the weak bosons turn into a degenerate multiplet ($M_Z = M_W = gv/2$, at LO), the W^3-B mixing vanishes ($\tan\theta_W = g'/g = 0$, at LO), and amplitudes with photons become zero (since $e = g'\cos\theta_W = 0$, at LO). Custodial symmetry breaking corrections are proportional to $\sin^2\theta_W \sim 0.2$, which makes the isospin limit scenario a suitable first approximation to the problem. In the following section, we will go beyond this limit and consider the numerical relevance of the $g' \neq 0$ corrections.

Nonetheless, for the purpose of the phenomenological analyses in this article, we will never consider the true isospin limit, which also requires $M_t = M_b$. While it has been used for some theoretical checks of the analytical expressions, the large experimental hierarchy $M_t \gg M_b$ is crucial for the numerical studies of the cross section and any comparison with the experiment.

For this work, we will assume a 10% deviation on the parameters of the effective Lagrangian. The relevant effective couplings for the present one-loop computation are a (hWW), b ($hhWW$), d_3 (hhh), and c_1 ($t\bar{t}h$), with their corresponding vertices within the parentheses. While the experimental values of a and c_1 fall within this range [28,29], b and d_3 present a much wider uncertainty [30]. Since the aim of this study is to call attention to the often neglected fermion corrections which are proportional to c_1, we will not use its precise experimental range. A 10% deviation from the SM already shows their relevance and the need to include them in future calculations.

Concerning the center-of-mass energy, we have considered the interval $0.5\ \mathrm{TeV} \leq \sqrt{s} \leq 3\ \mathrm{TeV}$, which is the relevant one to look for NP at the LHC. We will use as inputs $M_W = 80.38$ GeV, $M_Z = 91.19$ GeV, $M_H = 125.25$ GeV, $v = 246.22$ GeV, $M_t = 172.76$ GeV, and $M_b = 4.18$ GeV [10]. The value of the Weinberg angle is found in the standard way from M_W and M_Z, $\cos^2\theta_W = M_W^2/M_Z^2$ at LO.

A. $J = 0$ PWA: R_0

In the following plots, we have scanned the value of R_0 in the aforementioned region of the coupling space one parameter at a time while keeping the others fixed to their SM values for reference.

As we see in Figs. 2(a) and 2(b), when we explore a and b, respectively, we find $\mathcal{O}(10\%)$ corrections around $\sqrt{s} = 500$ GeV. For $\sqrt{s} \gtrsim 1.5$ TeV, bosons completely dominate, as expected. When it comes to the dependence on c_1, we can see [in Fig. 2(c)] 22% corrections at $\sqrt{s} \sim 3$ TeV when c_1 deviates from the SM. If we considered a broader phenomenological range for c_1, this correction would be even larger. For the case of d_3, we observe in Fig. 2(d) fermion corrections of the order of 8% around 500 GeV. Although in absolute terms R_0 barely changes with d_3, it decreases when the center-of-mass energy is increased. This lack of sensitivity is due to the fact that d_3 enters only in the hh cut and via a nonderivative interaction.

From this analysis, we extract that for R_0 the most relevant parameter is c_1. The further it is from its SM value, the larger the fermion contribution is, as expected from the analytical expression of the fermionic cuts.

It is also illustrative to show how each cut contributes to the total amplitude. These cumulative relative amplitude curves χ for the SM are shown in Fig. 3. Each curve contains the contribution of all intermediate cuts below the mentioned cut. They are ordered according to the value of the mass threshold of the intermediate state: The first cut is $b\bar{b}$, then WW and ZZ at the same energy ($g' = 0$), Zh, hh, and finally $t\bar{t}$. Clearly, in the SM case, in Fig. 3, top loop corrections are relevant only around $\sqrt{s} \sim 500$ GeV, reaching a maximum of $R_0 \sim 10\%$. The $b\bar{b}$ cut is present (blue line at the bottom), but its contribution is absolutely negligible for $J = 0$.

Now aware that d_3 is not relevant, we will explore the cumulative curves for BSM scenarios where a, b, and c_1 have been modified one at a time. As seen in Fig. 4, WW, ZZ, and hh provide a large section of the total amplitude

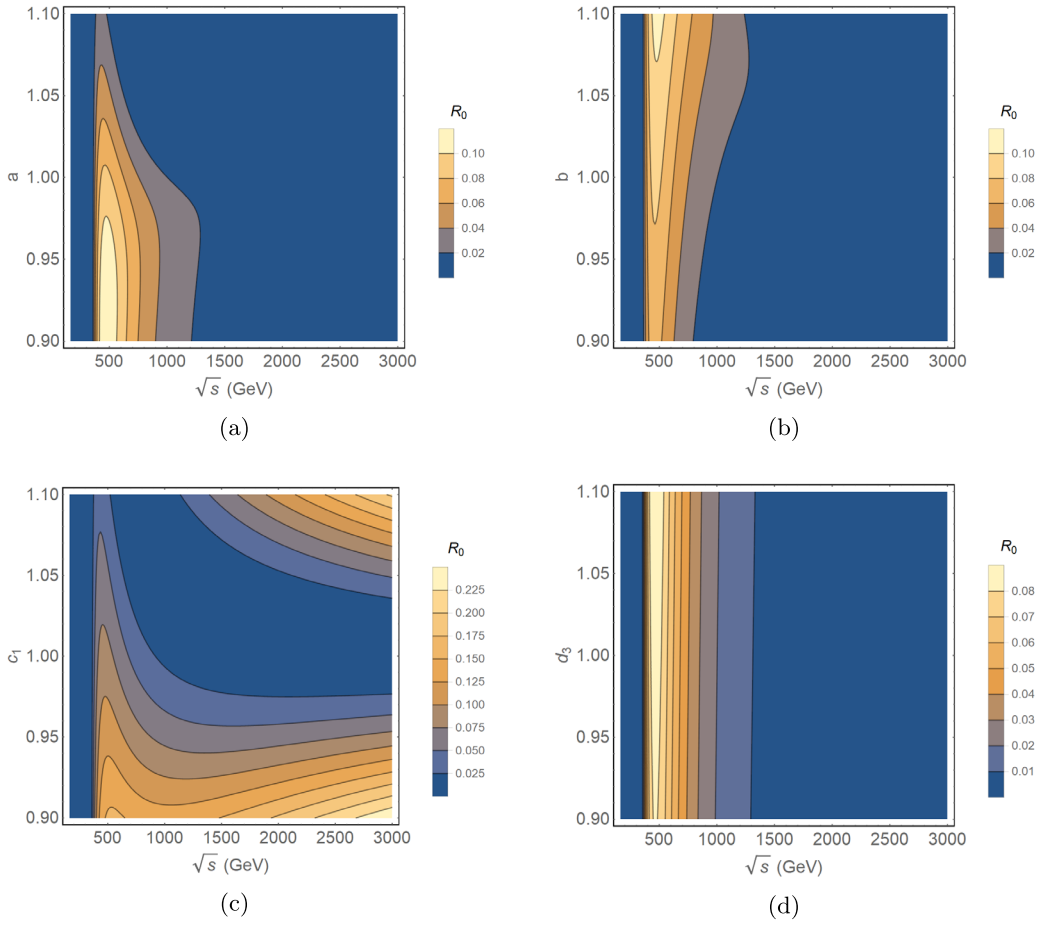

FIG. 2. (a) R_0 dependence on a for $b = c_1 = d_3 = 1$. (b) R_0 dependence on b for $a = c_1 = d_3 = 1$. (c) R_0 dependence on c_1 for $a = b = d_3 = 1$. (d) R_0 dependence on d_3 for $a = b = c_1 = 1$.

[Figs. 4(d)], while $t\bar{t}$ is important (corrections of the order of 22%) only when c_1 takes extreme values ($c_1 = 0.9$ or $c_1 = 1$) and the rest of the parameters are set to their SM values [Figs. 4(e) and 4(f)]. The Zh cut is relevant only below $\sqrt{s} \sim 500$ GeV and then rapidly becomes insignificant, as can be seen in Fig. 4.

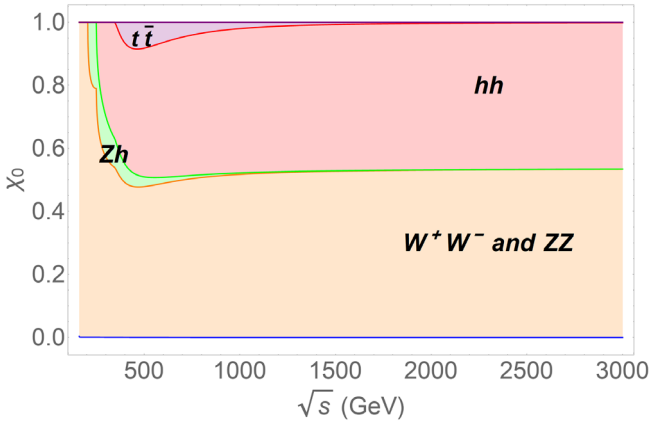

FIG. 3. Cumulative relative contribution of each channel to $J = 0$ PWAs in the SM.

These previous plots give us a notion of the behavior of the amplitude at different energies and values of the HEFT parameters. Now, we will explore the whole possible range these parameters can take to find a set which maximizes R_0. We will do this for two benchmark energies: 1.5 and 3 TeV, a pair of typical energies at which NP is usually expected. We scanned the space of effective parameters (a, b, c_1, d_3) within the aforementioned 10% deviation from the SM and located the point that maximized R_0 at a given c.m. energy $\sqrt{s}$. We find that $a = 1.023$, $b = 1.100$, $c_1 = 0.900$, and $d_3 = 1.100$ give rise to a $R_0 = 75\%$ at 1.5 TeV and $a = 1.008$, $b = 1.035$, $c_1 = 1.100$, and $d_3 = 0.900$ to a $R_0 = 94\%$ at 3 TeV. Some optimal couplings are found to lie on the boundaries of the considered parameter space due to the structure of their analytical expression in the amplitude. We have plotted the relative ratio for both of these configurations in Fig. 5. As seen in these optimal cases, fermion-loop corrections provide most of the amplitude for $J = 0$.

To test the sensitivity of R_0 to these optimal points (a, b, c_1, d_3), we have plotted R_0 by varying one parameter at a time while keeping the others fixed to the values that maximize R_0. This is shown in Fig. 6 for 3 and 1.5 TeV,

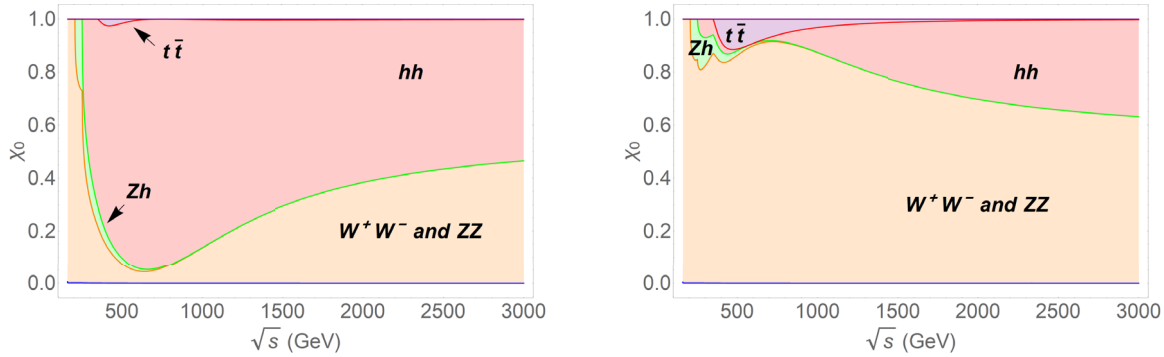

(a) $a = 1.10$ and $b = c_1 = d_3 = 1$.

(b) $a = 0.90$ and $b = c_1 = d_3 = 1$.

(c) $b = 1.10$ and $a = c_1 = d_3 = 1$.

(d) $b = 0.90$ and $a = c_1 = d_3 = 1$.

(e) $c_1 = 1.10$ and $a = b = d_3 = 1$.

(f) $c_1 = 0.90$ and $a = b = d_3 = 1$.

FIG. 4. Cumulative relative contributions for each absorptive cut to the $J = 0$ PWAs for a, b, and c_1 at the borders of the considered parameter space. The $b\bar{b}$ contribution is numerically negligible for this PWA.

respectively. The full dots on each curve represent the optimal value of the parameter which maximizes the ratio. We can observe that the R_0 correction rapidly drops if we change one of the values of a, b, and c_1. Thus, a fine interplay is needed among the couplings to produce these large fermion-loop corrections. Again, R_0 remains essentially constant with respect to d_3 variations.

In summary, it is possible to say that, in general, the assumption of neglecting the imaginary part of top-quark-loop corrections for the $J = 0$ channel is not well sustained, since we have found many sets of values of the HEFT parameters which yield meaningful contributions. Moreover, in some cases they even dominate the total amplitude.

B. $J = 1$ PWA: R_1

Now we consider the $J = 1$ PWAs. The only diagrams from fermion loops which yield a nonzero contribution to $J = 1$ do not involve a Higgs; hence, they do not contain any NP parameter (i.e., deviations from SM). Hence, fer_1 does not depend on the c_1 parameter and is fully determined by the SM gauge-fermion interactions. On the other hand, the bosonic part bos_1 depends only on a through the WW, ZZ, and Zh intermediate channels (the isoscalar hh channel does not contribute to $J = 1$). As can be seen in Fig. 7, we find a wide range of corrections for low energies (30%–40% at 0.5 TeV for $0.9 \lesssim a \lesssim 1.1$) and for high energies (10%–15% at 3 TeV in the whole range of a).

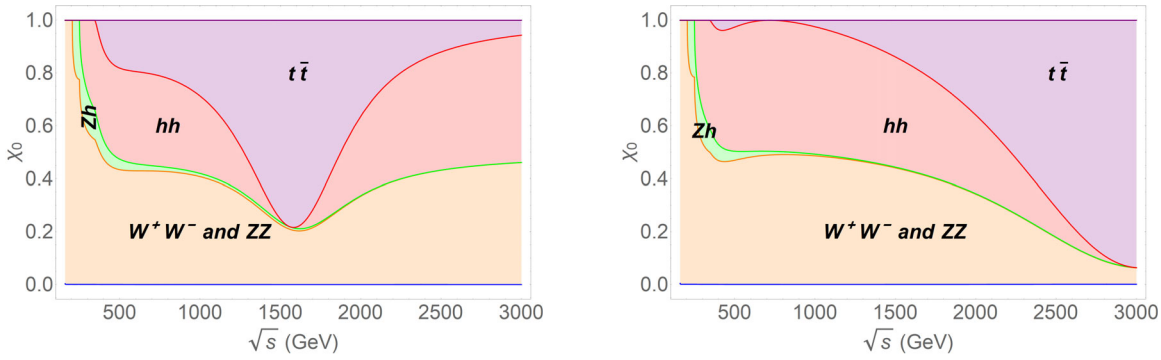

FIG. 5. (a) $J = 0$ PWAs: largest fermion-loop contribution of 75% found at 1.5 TeV for $a = 1.023$, $b = 1.100$, $c_1 = 0.900$, and $d_3 = 1.100$. (b) $J = 0$ PWAs: largest fermion-loop contribution of 94% found at 3 TeV for $a = 1.008$, $b = 1.035$, $c_1 = 1.100$, and $d_3 = 0.900$.

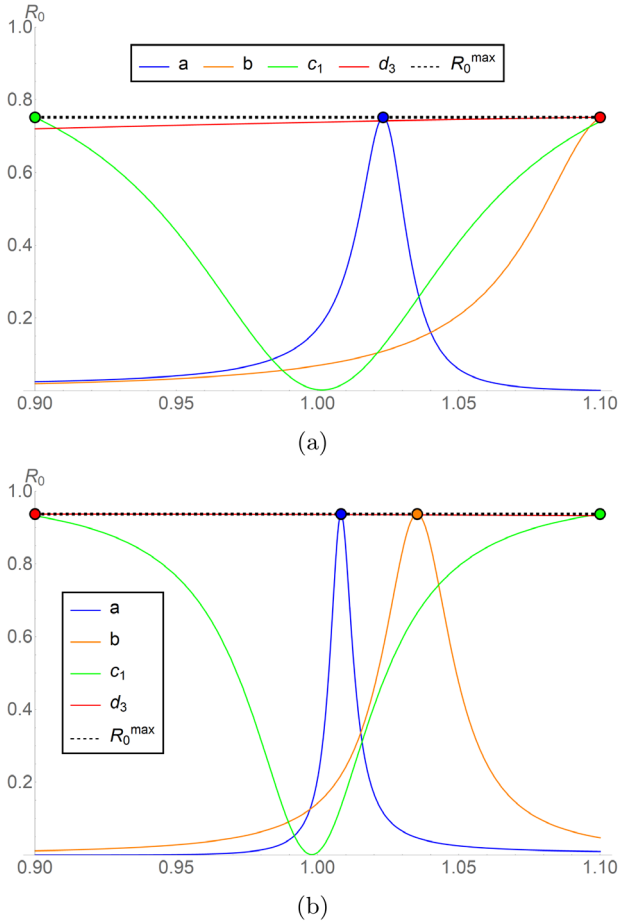

FIG. 6. Sensitivity of R_0 to each parameter when the rest are set to the highest correction value at $\sqrt{s} = 1.5$ TeV (top) and $\sqrt{s} = 3$ TeV (bottom).

In addition to WW and ZZ cuts, this $J = 1$ PWA also receives contributions from the Zh absorptive channel, even for $g' = 0$. The present work completes previous preliminary studies [9,14], which neglected the Zh channel on the basis of NET and custodial symmetry arguments. This channel yields, indeed, a large contribution to the amplitude, as can be seen in Figs. 8 and 9. This outcome is notable, as the Zh channel is usually not included when studying WW scattering. Since the only available HEFT parameter is a, we can easily describe the dependence of R_1 on NP. Values of a close to 1 minimize the boson contribution, thus yielding a high R_1. Since the $W^+W^- \to Zh$ tree-level scattering vanishes in the naive ET at lowest order in the chiral expansion, one needs to go beyond it to actually address this important boson-loop contribution.

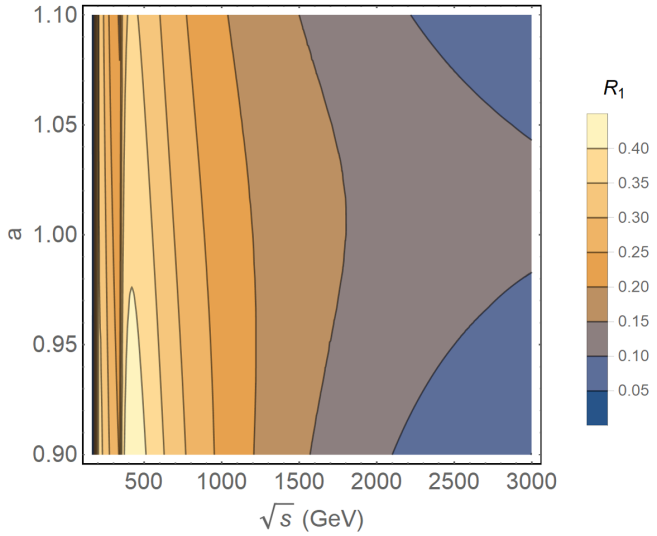

FIG. 7. R_1 dependence on the a parameter.

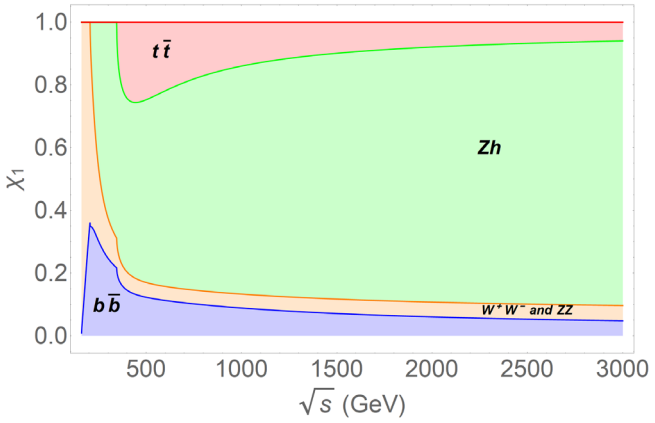

FIG. 8. Cumulative relative contribution of each channel to $J = 1$ PWAs in the SM.

For this partial wave, we can see in Figs. 8 and 9 that the $b\bar{b}$ cut provides a significant contribution to the total amplitude. Especially at large energies, the contribution from both cuts $t\bar{t}$ and $b\bar{b}$ are similar. In order to obtain a relevant fermion-loop contribution at high energies to the $J = 1$ channel from a quark doublet, at least one of the fermions needs to be heavy.

If we look for the optimal value of a that maximizes R_1 at the same benchmark energies as before, we encounter that $a = 0.991$ yields $R_1 = 17\%$ at 1.5 TeV and $a = 1.013$ yields $R_1 = 11\%$ at 3 TeV. In Fig. 10, we show the cumulative relative amplitudes of each cut for these benchmark energies. These values of a minimize the total boson-loop contribution at the mentioned c.m. energies (WW, ZZ, and Zh cuts), giving more relevance to the fermion cuts.

In Fig. 11, we can see the optimal points for both curves. The dependence on one parameter is also very revealing; even if we restrict ourselves to scenarios very close to the SM, we observe that both curves do not change dramatically. This is interesting, because, unlike the $J = 0$ case where we needed a fine interplay among the HEFT parameters, Fig. 11 shows significant fermion corrections

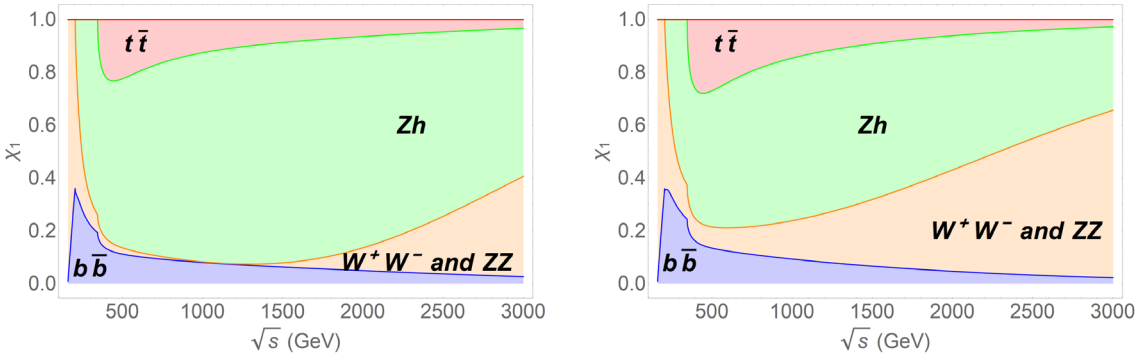

(a) (b)

FIG. 9. Cumulative relative contribution of each channel to the $J = 1$ PWAs for $a = 1.100$ (left) and $a = 0.900$ (right).

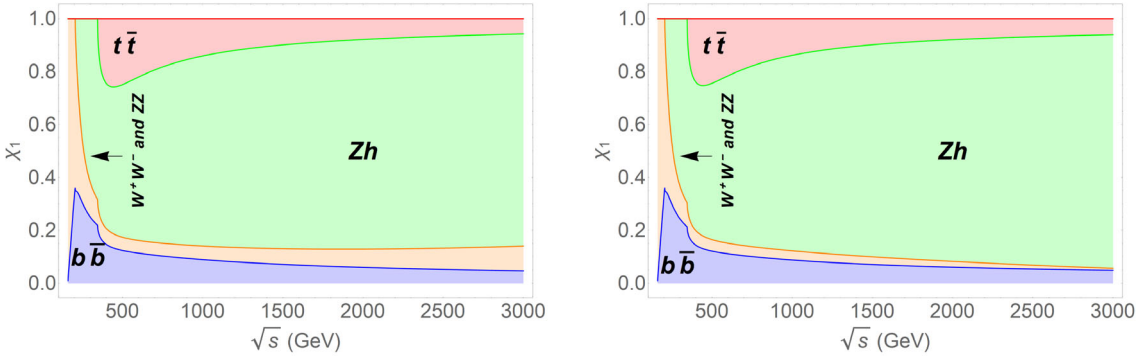

(a) $J = 1$ PWA: largest fermion-loop contribution of 17% at 1.5 TeV for $a = 0.991$.

(b) $J = 1$ PWA: largest fermion-loop contribution of 11% at 3 TeV for $a = 1.013$.

FIG. 10. (a) $J = 1$ PWA: largest fermion-loop contribution of 17% at 1.5 TeV for $a = 0.991$. (b) $J = 1$ PWA: largest fermion-loop contribution of 11% at 3 TeV for $a = 1.013$.

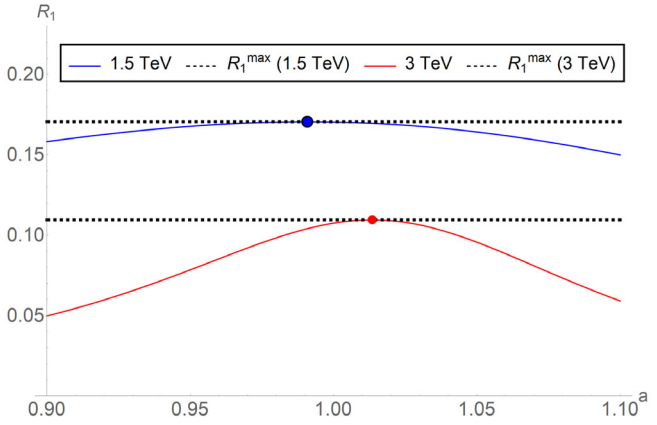

FIG. 11. Sensitivity of R_1 to the a parameter for the highest contribution at $\sqrt{s} = 1.5$ TeV and $\sqrt{s} = 3$ TeV.

above 5% (15%) for $\sqrt{s} = 1.5$ TeV ($\sqrt{s} = 3$ TeV) in the whole range of a studied here.

As was the case for the previous partial wave, neglecting fermion-loop corrections is not appropriate according to our work. Even if we restrict ourselves for scenarios close to the SM one where $a \approx 1$, we find significant fermion corrections.

V. FERMION LOOPS BEYOND THE $g' = 0$ LIMIT: PSEUDO-PWAs

A. $J = 0$ pseudo-PWA: R_0'

Moving to the more realistic case $g' \neq 0$, we have additional cuts: $\gamma\gamma$, γh, and γZ. As mentioned before, the integration has been performed only in the $|\cos\theta| \leq 0.9$ region due to a divergence in the t channel of the WW cut.

Thus, strictly speaking, these are not partial waves so we will refer to them as p-PWAs. Apart from this, the analysis will be analogous to the $g' = 0$ case.

As seen in Fig. 12, the contour plots do not dramatically change from the $g' = 0$ case. Areas around $\sqrt{s} \sim 500$ GeV are enhanced around 10% for Figs. 12(a) and 12(b) and 5% for Fig. 12(d) (sensitivity to a, b, and d_3, respectively). On the other side, when it comes to the sensitivity to c_1, shown in Fig. 12(c), we find larger contributions: from 20% around $\sqrt{s} \sim 500$ GeV up to 70% at 3 TeV when $c_1 = 0.9$ and $c_1 = 1.1$. Finally, the dependence on d_3 is negligible just like in the $g' = 0$ case, being relevant only for $\sqrt{s} \sim 500$ GeV.

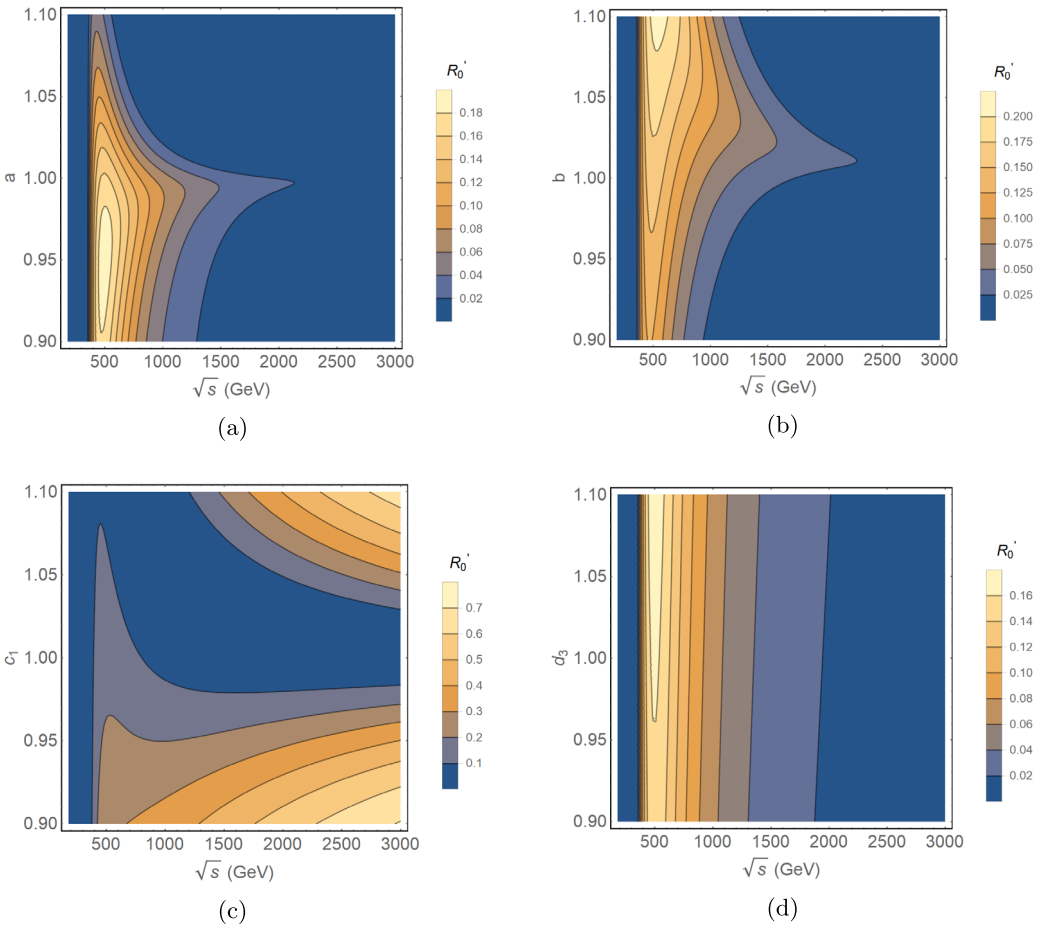

FIG. 12. (a) R_0' dependence on a for $b = c_1 = d_3 = 1$. (b) R_0' dependence on b for $a = c_1 = d_3 = 1$. (c) R_0' dependence on c_1 for $a = b = d_3 = 1$. (d) R_0' dependence on d_3 for $a = b = c_1 = 1$.

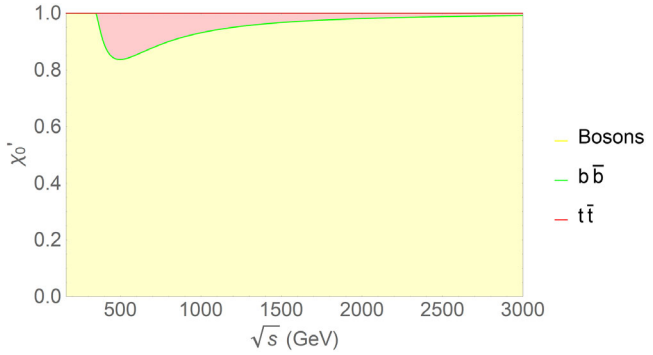

FIG. 13. Cumulative amplitude ratio for the $J = 0$ p-PWAs in the SM.

Given the numerous absorptive cuts we have now (nine in total, two fermionic and seven bosonic), the cumulative ratios are difficult to read from one plot, so we have subsumed all boson cuts here. In Fig. 13, we can see the corresponding cumulative relative ratios $\chi_i^{0'}$ for the SM. We observe that in the SM the fermion contributions are not relevant and can be neglected, as in the $g' = 0$ case. In Fig. 14, we show the $\chi_i^{0'}$ cumulative ratios for a and c_1 on the borders of the parameter space. Again, the most important parameter is c_1, giving rise to corrections of the order of 60% and 70% at 3 TeV when it reaches 1.1 and 0.9, respectively.

If we find the set of parameters which maximizes the fermion corrections, we have $R_0' = 80\%$ for $a = 1.011$, $b = 1.045$, $c_1 = 0.900$, and $d_3 = 1.094$ at 1.5 TeV and $R_0' = 93\%$ for $a = 1.003$, $b = 1.011$, $c_1 = 1.100$, and $d_3 = 1.100$ at 3 TeV. The contributions for each benchmark

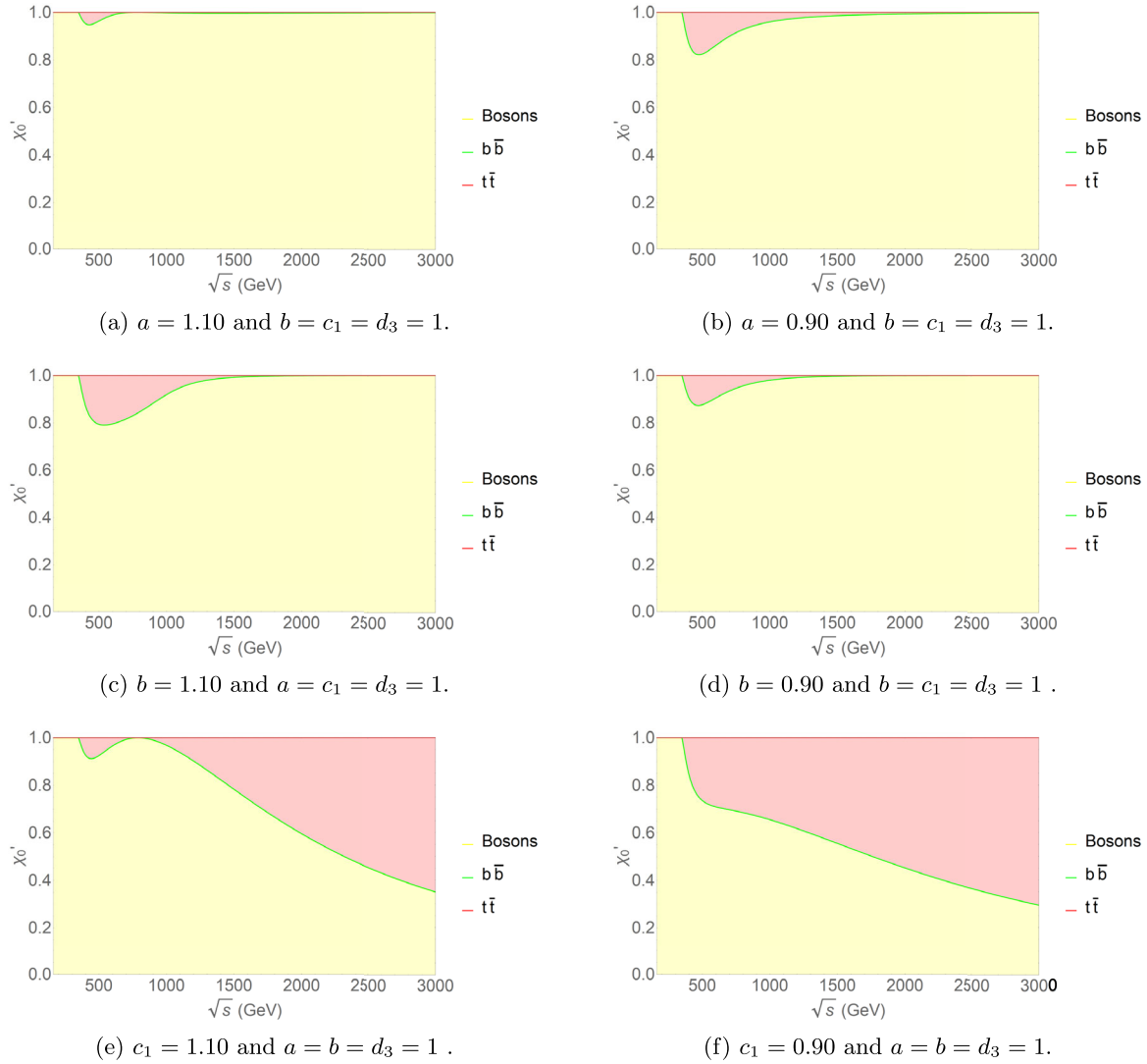

(a) $a = 1.10$ and $b = c_1 = d_3 = 1$.

(b) $a = 0.90$ and $b = c_1 = d_3 = 1$.

(c) $b = 1.10$ and $a = c_1 = d_3 = 1$.

(d) $b = 0.90$ and $b = c_1 = d_3 = 1$.

(e) $c_1 = 1.10$ and $a = b = d_3 = 1$.

(f) $c_1 = 0.90$ and $a = b = d_3 = 1$.

FIG. 14. Cumulative relative contributions for each absorptive cut to the $J = 0$ p-PWAs for a, b, and c_1 at the borders of the considered parameter space. The $b\bar{b}$ contribution is numerically negligible for this p-PWA.

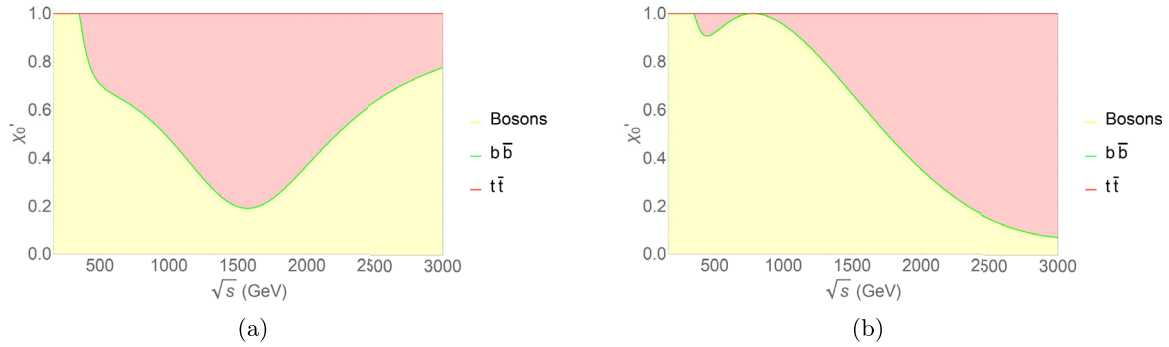

FIG. 15. (a) $J = 0$ p-PWAs: largest fermion-loop contribution of 80% for $J = 0$ at 1.5 TeV for $a = 1.011$, $b = 1.045$, $c_1 = 0.900$, and $d_3 = 1.094$. (b) $J = 0$ p-PWAs: largest fermion-loop contribution of 93% for $J = 0$ at 3 TeV for $a = 1.003$, $b = 1.011$, $c_1 = 1.100$, and $d_3 = 1.100$.

energy are shown in Fig. 15. Again, if we test the sensitivity of R_0' to these optimal parameters, we find that, in order to produce large fermion-loop corrections, one needs a fine interplay among the couplings. This is shown in Fig. 40 (in Appendix D 3 for the sake of clarity), and it is essentially similar to the previous R_0 results in Fig. 6.

From the plot it is clear that, for the $J = 0$ p-PWAs, fermion-loop corrections should not be neglected at high energies. They can provide a large contribution to the amplitude, even if one has several additional bosonic cuts in the $g' \neq 0$ case (e.g., $\gamma\gamma$).

B. $J = 1$ pseudo-PWA: R_1'

The contour plot for the next p-PWA, $J = 1$, is shown in Fig. 16. In this case, the behavior of R_1' around the SM is qualitatively similar to R_1, but the corrections are dramatically enhanced. We find $R_1' \sim 60\%$ from 0.5 to 3 TeV in the neighborhood of the SM.

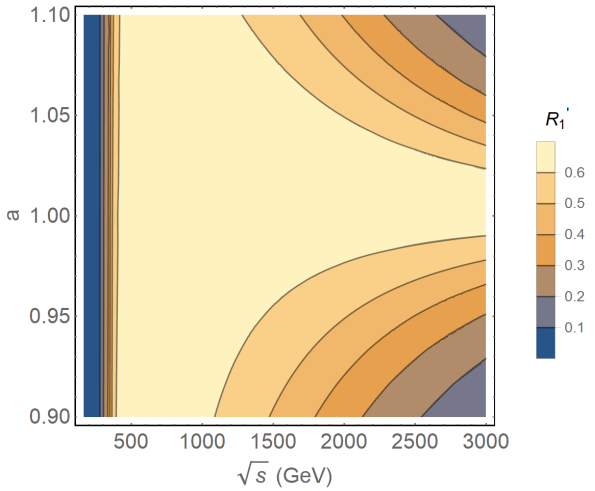

FIG. 16. R_1' dependence on the a parameter.

In Fig. 17, we see again that in the SM both fermions provide almost 70% of the amplitude from 500 GeV on when $a = 1$. In comparison, for $a = 1.1$ and $a = 0.9$, they reach a maximum around 500 GeV, and they rapidly decrease to around 15% at 3 TeV, as can be seen in Fig. 18.

As for R_1, the p-PWA ratio R_1' depends only on a. We then look for the point in parameter space that maximizes R_1'. The optimal values of a for 1.5 and 3 TeV are $a = 1.019$ (with $R_1' = 66\%$) and $a = 1.007$ (with a $R_1' = 67\%$), respectively (see Fig. 19).

If we test the sensitivity of R_1' to these optimal parameters, we find in Fig. 41 (in Appendix D 4 for the sake of clarity) that fermion contributions remain sizable for the whole range of a studied here. These are essentially the same conclusions found for R_1 in Fig. 11.

Again, values close to $a = 1$ yield significant fermion-loop corrections. These are of the order of 60% for the optimal value of a, around 3 times larger than the optimal value for R_1. Hence, in the case of angular cuts (e.g., $|\cos\theta| \leq 0.9$), top and bottom intermediate channels should not be neglected.

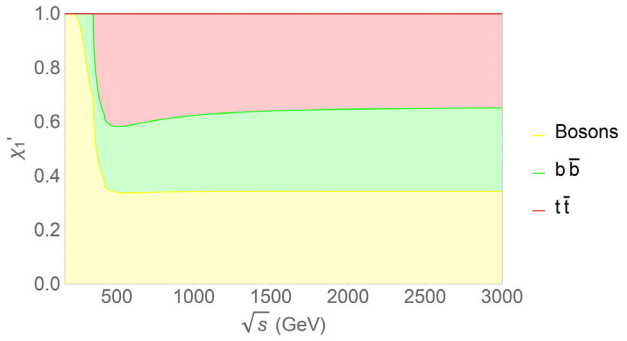

FIG. 17. Cumulative relative contribution of each channel to $J = 1$ p-PWAs in the SM.

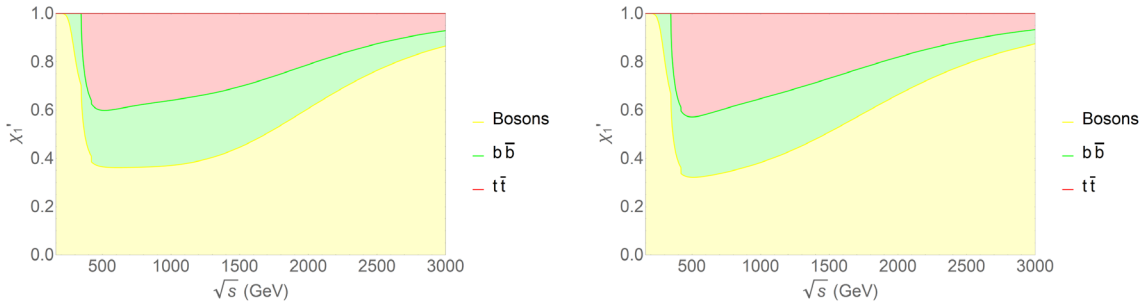

(a) (b)

FIG. 18. Cumulative relative contribution of each channel to the $J = 1$ p-PWAs for $a = 1.10$ (left) and $a = 0.90$ (right).

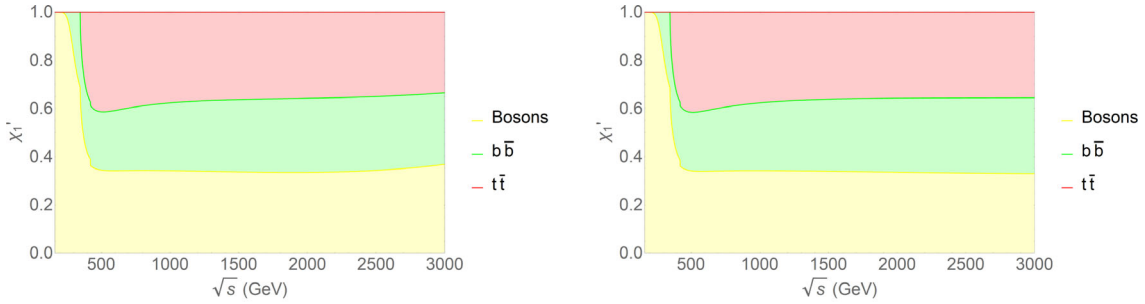

(a) (b)

FIG. 19. (a) $J = 1$ p-PWA: largest fermion-loop contribution of 66% at 1.5 TeV to $J = 1$ for $a = 1.019$. (b) $J = 1$ p-PWA: largest fermion-loop contribution of 67% at 3 TeV to $J = 1$ for $a = 1.007$.

VI. SPECIFIC SCENARIO: MINIMAL COMPOSITE HIGGS MODEL

When it comes to the importance of fermionic cuts, it is clear that they are relevant for some regions of the coupling space. Although these couplings could, in principle, take any value, we would like to be able to link them to specific NP scenarios where, in general, all effective parameters deviate from the SM in the particular way established by the model. For illustration, we will study here the $SO(5)/SO(4)$ minimal composite Higgs model (MCHM) [31], where the Higgs is a pseudo-Goldstone boson of an underlying strongly coupled theory. In this model, the couplings depend explicitly on the characteristic MCHM scale f.

The expressions for the relevant couplings for our analysis are [31,32]

$$a^* = c_1^* = d_3^* = \sqrt{1-\xi}, \quad b^* = 1-2\xi, \quad \text{with} \quad \xi = v^2/f^2.$$

Because of the structure of the MCHM, only values smaller than 1 are allowed for these effective couplings. Note that the four HEFT couplings are determined by the NP scale f. We have then computed the previous PWAs and p-PWAs for various values of f within this model. To ease the analysis, we will provide the corresponding value of the hWW coupling a together with f in the labels of the different curves (Figs. 20–23). For $0.90 \leq a^* \leq 1.00$, this implies $f \geq 0.56$ TeV, with $a^* \to 1$ for $f \to \infty$.

A. Limit $g' = 0$

We have plotted the ratios R_0 and R_1 as a function of $\sqrt{s}$ for different values of f in Figs. 20 and 21, respectively.

As it can be seen in Fig. 20, R_0 is drastically changed. Below the threshold of $t\bar{t}$ production, only $b\bar{b}$ is present, but

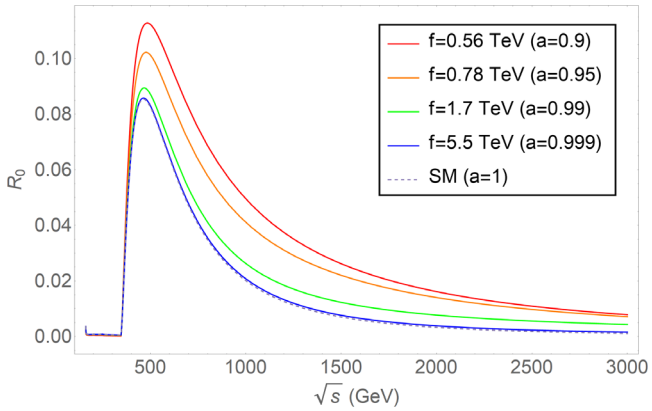

FIG. 20. Ratio for the R_0 PWAs in the MCHM.

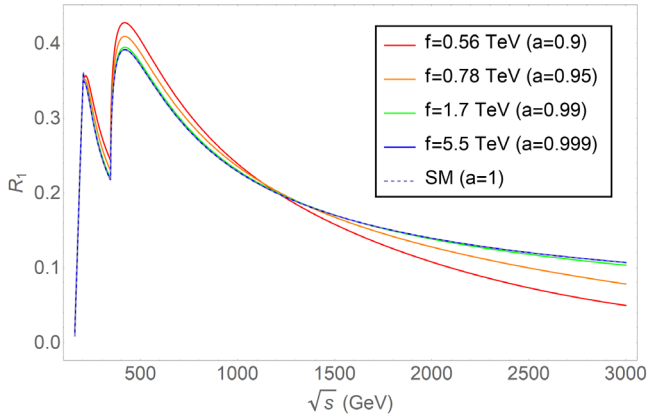

FIG. 21. Ratio for the R_1 PWAs in the MCHM.

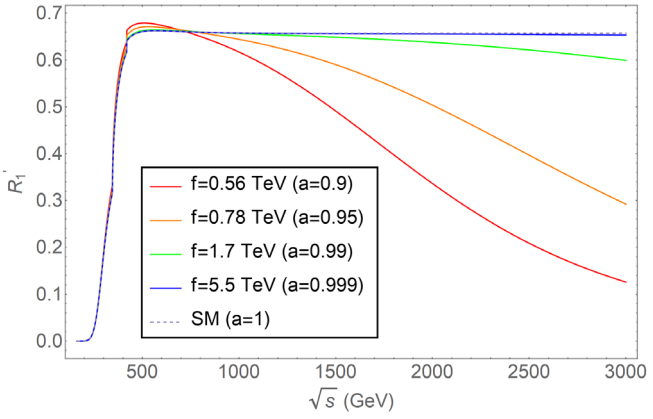

FIG. 23. Ratio for the R_1' PWAs in the MCHM.

its contribution is negligible. R_0 rapidly increases when top corrections enter at $\sqrt{s} \simeq 350$ GeV. In the present study, we find the maximum value $R_0 = 11\%$ for $a^* = 0.9$, at the boundary of our allowed range. It then quickly decreases for larger values of a^* at all energies.

The SM curve provides the lowest limit for the fermion correction, while the $a^* = 0.9$ curve provides the upper bound.

For R_1 (see Fig. 21), we observe a similar behavior. When the $t\bar{t}$ cut appears, R_1 reaches a maximum of 41% around 500 GeV for an $a^* = 0.9$. Again, all curves decrease rapidly, but the behavior at large energies is different. In this case, the SM curve provides the largest fermion correction, while the $a^* = 0.9$ curve the smallest ones.

In summary, in both R_0 and R_1 cases, when we restrict ourselves to the MCHM, the largest corrections appear always at $\sqrt{s} \sim 500$ GeV, with $a^* = 0.9$ the value that maximizes fermion corrections at that energy point. At large energies, $\sqrt{s} \sim 3$ TeV, R_0 becomes negligible (maximum $R_0 \sim 1\%$) for $a^* = 0.9$, while R_1 presents a significant contribution (maximum $R_1 \sim 10\%$) for $a = 1$.

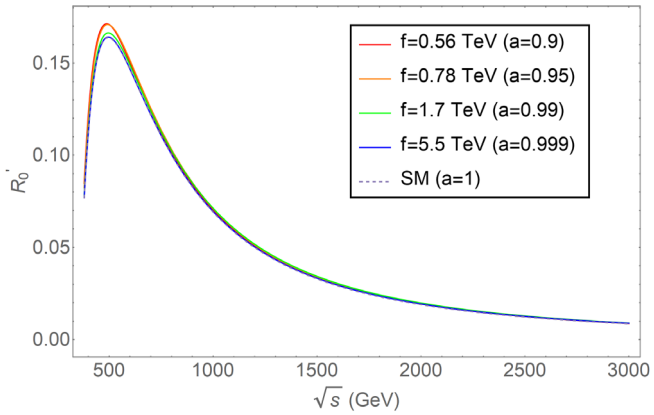

FIG. 22. Ratio for the R_0' PWAs in the MCHM.

B. Beyond the $g' = 0$ limit

As can be seen in Fig. 22, the result for R_0' is very similar to R_0 in the $g' = 0$ case; the largest fermion contribution is found around $\sqrt{s} \sim 500$ GeV, being around 17%. At high energies, the R_0' decreases rapidly, becoming negligible.

For R_1' we note an interesting behavior. As in the R_1 analysis, we find a maximum for R_1' around 500 GeV but somewhat larger ($R_1' \sim 65\%$). However, as we increase the energy, there are curves with coupling values close to the SM which decrease very slowly with the c.m. energy. This shows that the amplitudes depend highly on the angular cut, as was mentioned for the $W^+W^- \to W^+W^-$ corrections in Ref. [33]. Again, the maximum contribution is found for the SM curve at high energies and is about 65%.

VII. CONCLUSIONS

In this work, we have pondered in detail the widespread assumption that fermion-loop corrections can be neglected at high energies within the HEFT framework. For this, we have compared the imaginary part arising from top- and bottom-quark loops and that from boson loops in the elastic $W^+W^- \to W^+W^-$ scattering. We have included all intermediate channels and all possible polarization states not included in previous preliminary works [9,14].

In order to analyze the importance of fermion loops, we have computed the ratios R_0 and R_1 for the first partial-wave amplitudes, $J = 0$ and $J = 1$, respectively. R_J close to 0 indicates a dominance of boson loops, whereas a value close to 1 points out that fermion cuts dominate.

Because of the presence of infrared divergences in boson-loop diagrams (WW cut) where the momentum of a t-channel photon goes to zero, a full angular projection onto PWAs is not possible. In order to deal with the PWAs and to project onto the full angle domain, we have considered two approaches: (1) Set $g' = 0$, which removes photon interactions and, hence, the infrared divergent diagrams; (2) keep $g' \neq 0$ but impose an angular cut ($|\cos\theta| < 0.9$), which restricts the angular integration

avoiding the angular divergence. These two approaches give rise to the ratios R_J for the imaginary part of the PWAs with $g' = 0$ (approach 1) and the R'_J ratios for the imaginary part of the so-called pseudo-PWAs (approach 2). We have explored these two types of ratios, scanning the possible values of the relevant HEFT couplings. This has allowed us to assess the validity of the assumption of neglecting top- and bottom-quark loops.

In the first scenario, $g' = 0$, there are wide regions where the bosonic loop contributions are dominant as can be seen for the $J = 0$ PWA in Fig. 2. However, this is not the case in some ranges of the parameter space; large deviations of c_1 ($h\bar{t}t$ coupling) from the SM yield significant top-quark contributions. The $b\bar{b}$ contributions to $J = 0$ are not relevant as can be seen in Figs. 3 and 4, given the fact that they are proportional to M_b. For the $J = 1$ PWA, the same occurs when a (hWW coupling) is close to 1, as can be seen in Fig. 7. This minimizes the bosonic contribution and leads to a higher R_1. In this case, the $b\bar{b}$ cut yields a relevant contribution, as can be seen in Figs. 17 and 18. In particular, the amplitudes of both fermion cuts present a similar correction at high energies, showing that just one heavy quark in the EW doublet is enough to obtain significant corrections to the $J = 1$ PWA.

In the second scenario, $g' = 0$ with angular cuts, we find that the results for the $J = 0$ p-PWA R'_0 are similar to those for R_0, as one can see in Fig. 12. Large deviations of c_1 from the SM yield important top-quark contributions, again with negligible effects from the $b\bar{b}$ cut. For the $J = 1$ p-PWA. we observe a significant raise in the ratio R'_1 with respect to R_1. This can be seen in Fig. 16, indicating that the $J = 1$ partial-wave amplitude is highly dependent on angular cuts. Figure 17 shows a significant contribution to R'_1 from the $b\bar{b}$ cut, due to the same reasons discussed in the $g' = 0$ case for R_1 in Fig. 9.

There are also configurations for the four HEFT couplings (a, b, c_1, and d_3) which make these fermion contributions even more important. We summarize the largest corrections we have found for the PWAs and pseudo-PWAs in Tables I and II, respectively, $J = 0$ and $J = 1$. We have looked for the point in parameter space that maximizes fermion contributions at two benchmark energies: $\sqrt{s} = 1.5$ TeV and $\sqrt{s} = 3$ TeV. We have computed the sensitivity of these optimal HEFT coupling values by fixing three of them and varying one at a time. We can observe that there is a fine interplay of the couplings a, b, and c_1 which maximize R_0 and R'_0 for these benchmark energies (Figs. 6 and 40, respectively). One can also see that the value of d_3 is not relevant for the analysis. For $J = 1$, we find that values close to $a = 1$ minimize the bosonic contribution, yielding higher R_1 and R'_1 ratios (Figs. 11 and 41, respectively).

Based on what has been described above, we conclude that the assumption of neglecting the imaginary part of top- and bottom-quark-loop contributions to $W^+W^- \to W^+W^-$ in favor of the imaginary part of bosonic loops does not entirely hold. For the case $J = 0$, it is true there are wide ranges where fermion-loop contributions are negligible. However, this is false in some regions, where a ± 0.1 deviation of c_1 from 1 (SM) would give a 22% and 18% top-quark-loop contribution to R_0 and R'_0, respectively. Likewise, some configurations of a, b, c_1, and d_3 can make fermion loops even dominant, as shown in Table I. For $J = 1$, something similar occurs since we do not need to deviate so much from $a = 1$ (SM). Values of a close to 1 yield significant top- and bottom-quark-loop contributions to both PWAs and p-PWAs for $J = 1$, as shown in Table II.

For the MCHM case, we do not find meaningful contributions to the $J = 0$ ratios, as can be seen in Figs. 20 and 22. Both plots show maximums around 500 GeV, but the ratios decay rapidly with the c.m. energy. For $J = 1$, a value of $a = 1$ ($f \to \infty$ TeV) produces a maximum $R_1 = 10\%$ at 3 TeV, as can be seen in Fig. 21. When it comes to the $g' \neq 0$ case, given the strong dependence on the angular cut, R'_1 (Fig. 23) is enhanced and takes an almost constant value $R'_1 \approx 65\%$ for an hWW coupling close to the SM one ($a \approx 1$). Therefore, in the MCHM scenario, the imaginary top- and bottom-quark-loop corrections would enhance the $J = 1$ partial wave considerably more than the $J = 0$. Note that, in the MCHM, the HEFT relevant parameters need to be smaller than 1 due to their particular dependence on the NP scale f.

Currently, we are working on the full one-loop contribution [11]. We plan to complete the present computation with the real part of the one-loop amplitudes, where fermion contributions might also be important or even dominant, as we have found in some cases for the imaginary part.

TABLE I. Corrections to $J = 0$ PWAs for the $g' = 0$ case (first two rows) and the $J = 0$ p-PWAs (last two rows). In the second, third, fourth, and fifth columns, we provide, respectively, the values of a, b, c_1, and d_3 that maximize the fermion-loop contributions.

$\sqrt{s}$ (TeV)	$a-1$	$b-1$	c_1-1	d_3-1	$J=0$
1.5 (PWA)	0.023	0.100	−0.100	0.100	$R_0 = 76\%$
3 (PWA)	0.008	0.035	0.100	−0.100	$R_0 = 94\%$
1.5 (p-PWA)	0.011	0.045	−0.100	0.094	$R'_0 = 81\%$
3 (p-PWA)	0.003	0.011	0.100	0.100	$R'_0 = 93\%$

TABLE II. Corrections to $J = 1$ PWAs for the $g' = 0$ case (first two rows) and the $J = 1$ p-PWAs (last two rows). In the second column, we provide the value of a that maximizes the fermion-loop contributions.

$\sqrt{s}$ (TeV)	$a - 1$	$J = 1$
1.5 (PWA)	−0.009	$R_1 = 18\%$
3 (PWA)	0.013	$R_1 = 12\%$
1.5 (p-PWA)	0.019	$R_1' = 66\%$
3 (p-PWA)	0.007	$R_1' = 67\%$

Along with this, we plan to deal with the possibility of a strongly interacting electroweak symmetry breaking sector and the problem of unitarization of the whole amplitude for all VBS channels [11,34].

ACKNOWLEDGMENTS

We thank our collaborators A. Castillo, R. L. Delgado, and F. Llanes-Estrada, who participated in the earlier parts of the research presented in this article [12]. We also want to thank I. Asiáin, M. J. Herrero, and P. D. Ruiz-Femenía for useful discussions. This research is partly supported by the Ministerio de Ciencia e Inovación under research Grants No. FPA2016-75654-C2-1-P and No. PID2019–108655GB-I00/AEI/10.13039/501100011033; by the EU STRONG-2020 project under Program No. H2020-INFRAIA-2018-1 [Grant Agreement No. 824093]; and by the STSM grant from COST Action CA16108. C. Q.-C. has been funded by the MINECO (Spain) predoctoral Grant No. BES-2017-082408.

APPENDIX A: FEYNMAN DIAGRAMS

We show here the diagrams considered for the calculation of the imaginary one-loop contribution to $W^+W^- \to W^+W^-$ arising from a given particle in the loop. In order to do this, we will consider the tree-level contribution of $W^+W^- \to XY$ where X and Y can be $X, Y = W, Z, h, \gamma, t, b$ (see Figs. 24–32) and by perturbative unitarity calculate the imaginary part of the contribution due to loops of X, Y to $W^+W^- \to W^+W^-$.

This can be easily seen diagrammatically. Let us consider, for example, the tree-level process $W^+W^- \to \gamma\gamma$. The three diagrams contributing to this process are shown in Fig. 24.

Via perturbative unitarity, we can calculate the imaginary part of the loop contributions to $W^+W^- \to W^+W^-$ arising from photon loops. This can be achieved by taking each diagram in Fig. 24 and connecting it with the rest of them to yield the nine diagrams in Fig. 33. Although all nine diagrams contribute at one loop, only diagrams 1, 4, 5, 6, 7, and 8 in Fig. 33 contribute to the imaginary part through the absorptive cut in the s channel.

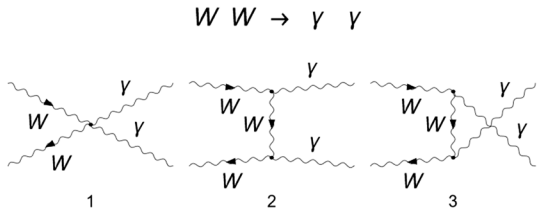

FIG. 24. Tree-level diagrams for $WW \to \gamma\gamma$.

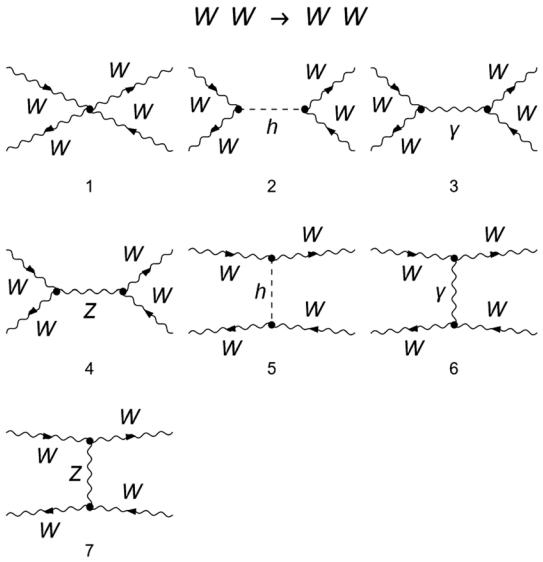

FIG. 25. Tree-level diagrams for $WW \to WW$.

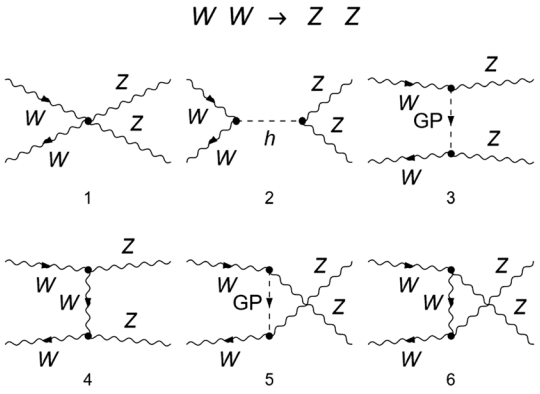

FIG. 26. Tree-level diagrams for $WW \to ZZ$, where GP refers to the positive would-be-Goldstone boson here and in the following diagrams.

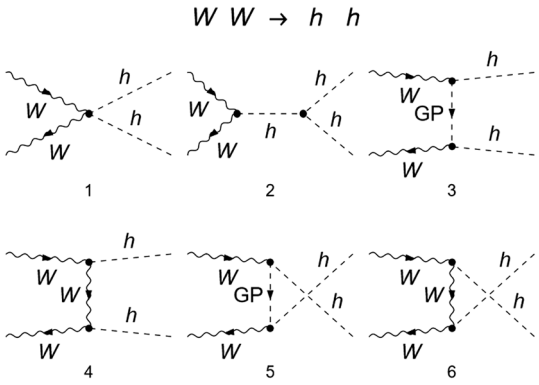

FIG. 27. Tree-level diagrams for $WW \to hh$.

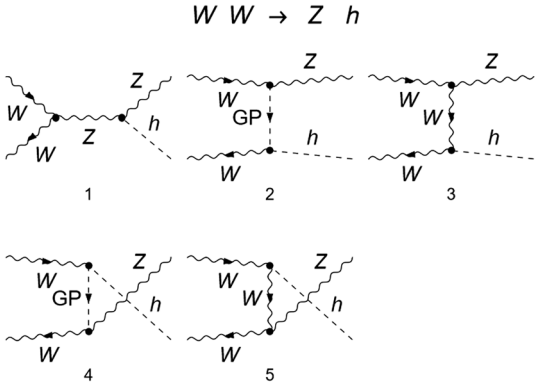

FIG. 28. Tree-level diagrams for $WW \to Zh$.

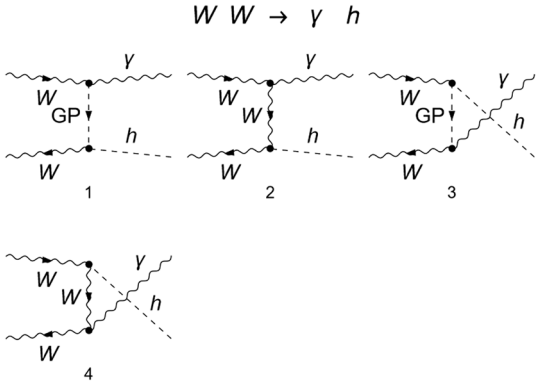

FIG. 29. Tree-level diagrams for $WW \to \gamma h$.

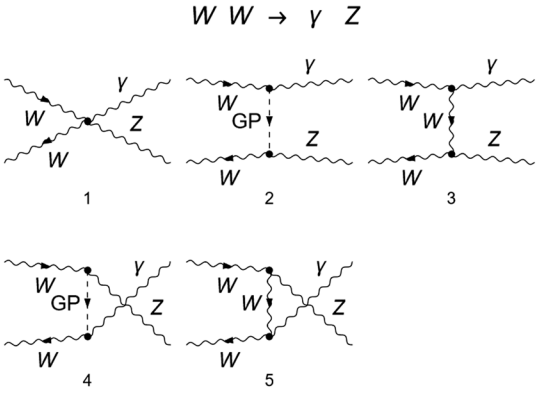

FIG. 30. Tree-level diagrams for $WW \to \gamma Z$.

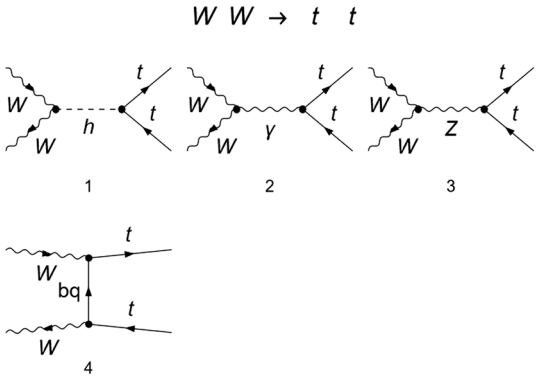

FIG. 31. Tree-level diagrams for $WW \to t\bar{t}$.

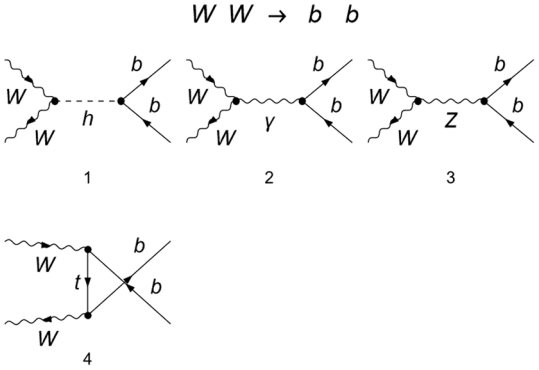

FIG. 32. Tree-level diagrams for $WW \to b\bar{b}$.

APPENDIX B: KINEMATICS

We present the following kinematics in the center-of-mass frame used to calculate the required processes. With this and the Mandelstam variables defined as usual, one should be able to obtain the amplitudes in Appendix C. In order to not repeat a large quantity of same polarization and momenta vectors, we will detail the polarization and momentum of only the new final states. For example, if one wants to calculate the amplitude $\mathcal{A}(W^+(p_1,\epsilon_1^L)W^-(p_2,\epsilon_2^L) \to \gamma(p_3,\epsilon_3^a)Z(p_4,\epsilon_4^b))$, one needs to use the polarization and momentum defined in Appendix B 4 for the photon and the polarization and momentum defined in Appendix B 3 for the Z boson. The only exception to this is the amplitude with fermions in the final state, where we use the momenta and polarizations for the W bosons detailed in Appendix B 5.

1. $W^+(p_1',\epsilon_1^{L'})W^-(p_2',\epsilon_2^{L'}) \to t(p_3,\lambda_3)\bar{t}(p_4,\lambda_4)$

For the special case of fermions in the final state, we will set their momenta in the z axis, facilitating the calculation of the

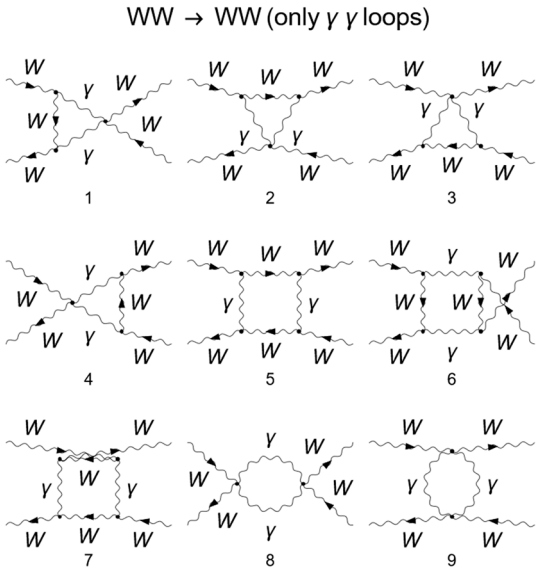

FIG. 33. Diagrams for $WW \to WW$ arising from loops of photons.

product of spinor chains. The angular dependence hence comes from the initial states of the W bosons.

As usual, θ is the angle between particles 1 and 3, ϕ is the azimuth angle, and $\epsilon_1^{L'}$ and $\epsilon_2^{L'}$ refer to the longitudinal polarization of the W bosons:

$$\begin{aligned} p_1{}' &= (E, |\vec{p}|\sin(\theta)\cos(\phi), |\vec{p}|\sin(\theta)\sin(\phi), |\vec{p}|\cos(\theta)), \\ p_2' &= (E, -|\vec{p}|\sin(\theta)\cos(\phi), -|\vec{p}|\sin(\theta)\sin(\phi), -|\vec{p}|\cos(\theta)), \\ p_3' &= (E_t, 0, 0, |\vec{p_t}|), \quad p_4' = (E_t, 0, 0, -|\vec{p_t}|), \end{aligned} \tag{B1}$$

$$\begin{aligned} \epsilon_1^{L'} &= \frac{E}{M_W}(|\vec{p}|, E\sin(\theta)\cos(\phi), E\sin(\theta)\sin(\phi), E\cos(\theta)), \\ \epsilon_2^{L'} &= \frac{E}{M_W}(|\vec{p}|, -E\sin(\theta)\cos(\phi), \\ &\quad -E\sin(\theta)\sin(\phi), -E\cos(\theta)), \end{aligned} \tag{B2}$$

$$u_3^+(p_3, M_t) = \begin{pmatrix} \sqrt{E_t - p_t} \\ 0 \\ \sqrt{p_t + E_t} \\ 0 \end{pmatrix}, \qquad u_3^-(p_3, M_t) = \begin{pmatrix} 0 \\ \sqrt{p_t + E_t} \\ 0 \\ \sqrt{E_t - p_t} \end{pmatrix},$$

$$v_4^+(p_4, M_t) = \begin{pmatrix} \sqrt{p_t + E_t} \\ 0 \\ -\sqrt{E_t - p_t} \\ 0 \end{pmatrix}, \qquad v_4^-(p_4, M_t) = \begin{pmatrix} 0 \\ \sqrt{E_t - p_t} \\ 0 \\ -\sqrt{p_t + E_t} \end{pmatrix}, \tag{B3}$$

where $u_3^{\lambda_3}$ and $v_4^{\lambda_4}$ are the spinors for the particle and antiparticle in the Weyl basis and λ_3 and λ_4 their polarizations, respectively.

2. $W^+(p_1, \epsilon_1^L) W^-(p_2, \epsilon_2^L) \to W^+(p_3, \epsilon_3^a) W^-(p_4, \epsilon_4^b)$

For the full bosonic case, since there is no angular dependence on the azimuth ϕ, we can set the momentum in the x-z plane to make the calculations easier:

$$\begin{aligned} p_1 &= (E, 0, 0, |\vec{p}|), \qquad p_2 = (E, 0, 0, -|\vec{p}|), \\ p_3 &= (E, |\vec{p_3}|\sin(\theta), 0, |\vec{p_3}|\cos(\theta), \\ p_4 &= (E, -|\vec{p_3}|\sin(\theta), 0, -|\vec{p_3}|\cos(\theta)), \end{aligned} \tag{B4}$$

$$\epsilon_1^L = \frac{1}{M_W}(|\vec{p}|, 0, 0, E), \qquad \epsilon_2^L = \frac{1}{M_W}(|\vec{p}|, 0, 0, -E), \tag{B5}$$

$$\begin{aligned} \epsilon_3^L &= \frac{1}{M_W}(|\vec{p}|, E\sin(\theta), 0, E\cos(\theta)), \\ \epsilon_4^L &= \frac{1}{M_W}(|\vec{p}|, -E\sin(\theta), 0, -E\cos(\theta)), \end{aligned} \tag{B6}$$

$$\begin{aligned} \epsilon_3^+ &= \frac{1}{\sqrt{2}}(0, \cos(\theta), i, -\sin(\theta)), \qquad \epsilon_3^- = \epsilon_3^{+*}, \\ \epsilon_4^+ &= \frac{1}{\sqrt{2}}(0, \cos(\theta), -i, -\sin(\theta)), \qquad \epsilon_4^- = \epsilon_4^{+*}, \end{aligned} \tag{B7}$$

where $\epsilon_{1,2}^L$ refer to the longitudinal polarization of the initial particles and $\epsilon_{3,4}^{+/-/L}$ refer to the polarization of particle 3 or 4 with positive, negative, or longitudinal polarization, respectively.

3. $W^+(p_1,\epsilon_1^L)W^-(p_2,\epsilon_2^L) \to Z(p_3,\epsilon_3^a)Z(p_4,\epsilon_4^b)$

For ZZ scattering, the positive and negative polarizations are given by the same vectors as for the WW case, except for the longitudinal modes which depend on the mass:

$$\epsilon_3^L = \frac{1}{M_Z}(|\vec{p}_3|, E_3\sin(\theta), 0, E\cos(\theta)),$$
$$\epsilon_4^L = \frac{1}{M_Z}(|\vec{p}_3|, -E_3\sin(\theta), 0, -E\cos(\theta)), \quad \text{(B8)}$$

$$p_3 = (E_3, |\vec{p}_3|\sin(\theta), 0, |\vec{p}_3|\cos(\theta)),$$
$$p_4 = (E_3, -|\vec{p}_3|\sin(\theta), 0, -|\vec{p}_3|\cos(\theta)), \quad \text{(B9)}$$

where E_3 is the energy of particle 3.

4. $W^+(p_1,\epsilon_1^L)W^-(p_2,\epsilon_2^L) \to \gamma(p_3,\epsilon_3^a)\gamma(p_4,\epsilon_4^b)$

The polarizations $\epsilon_{3,4}^{+-}$ refer to the positive and negative polarization of particle 3 and 4, respectively:

$$\epsilon_3^+ = \frac{1}{\sqrt{2}}(0, \cos(\theta), -i, -\sin(\theta)), \qquad \epsilon_3^- = \epsilon_3^{+*},$$
$$\epsilon_4^+ = \frac{1}{\sqrt{2}}(0, \cos(\theta), i, -\sin(\theta)), \qquad \epsilon_4^- = \epsilon_4^{+*}, \quad \text{(B10)}$$

$$p_3 = (E_3, |\vec{p}_3|\sin(\theta), 0, |\vec{p}_3|\cos(\theta)),$$
$$p_4 = (E_3, -|\vec{p}_3|\sin(\theta), 0, -|\vec{p}_3|\cos(\theta)). \quad \text{(B11)}$$

5. $W^+(p_1,\epsilon_1^L)W^-(p_2,\epsilon_2^L) \to h(p_3,)h(p_4)$

$$p_3 = (E_3, |\vec{p}_3|\sin(\theta), 0, |\vec{p}_3|\cos(\theta)),$$
$$p_4 = (E_3, -|\vec{p}_3|\sin(\theta), 0, -|\vec{p}_3|\cos(\theta)). \quad \text{(B12)}$$

APPENDIX C: SCATTERING AMPLITUDES

For the calculation of the $\mathcal{O}(p^4)$ one-loop W_LW_L elastic scattering beyond NET, we will need the $\mathcal{O}(p^2)$ (tree-level) W_LW_L amplitudes to all possible intermediate states, which are provided below. Since we are always dealing with longitudinal polarized electroweak gauge bosons in the initial state, we will label only the amplitudes with the polarization state of the final particles. Given the length of the analytic expression of some amplitudes, we will write the amplitude (without contracting) for each diagram in terms of the particle exchanged and the channels s, t, and u. For example, $\mathcal{A}_{\pi,t}$ means this diagram is exchanging a Goldstone-π in the channel t. Since we have performed the calculation in an arbitrary gauge, the various contributions to amplitudes contain the gauge parameters ξ_W, ξ_Z, and ξ_A. We have checked that the full amplitudes are gauge independent, but, for the sake of achieving compact expression when it comes to the polarized amplitudes, the expressions are shown in the unitary gauge.

All calculations have been performed by hand and checked via FeynArts [35], which generates all diagrams considered, and evaluated using FeynCalc [36]. For compactness, the amplitudes are written in terms of $x = \cos\theta$ and $\beta_X = \sqrt{1-4M_X^2/s}$.

1. $\mathcal{A}(W^+(p_1,\epsilon_1^L)W^-(p_2,\epsilon_2^L) \to t(p_3,\lambda_3)\bar{t}(p_4,\lambda_4))$

We will provide $t\bar{t}$ amplitude in terms of the diagrams involved, where P_R and P_L are the right and left chirality projectors, respectively, and N_C is the number of colors.

a. Amplitudes in terms of the polarization

$$\mathcal{A}_{H,s} = -ac_1\frac{(i\sqrt{N_c}gM_W\epsilon_1{}^\mu\epsilon_2{}^\nu\eta^{\mu\nu})}{(p_3+p_4)^2-M_H^2} \times (\bar{u_3}^{\lambda_3}(p_3,M_t)).\left(-\frac{igP_RM_t}{2M_W}-\frac{igP_LM_t}{2M_W}\right).(v_4^{\lambda_4}(p_4,M_t)), \quad \text{(C1)}$$

$$\mathcal{A}_{\gamma,s} = -i\sqrt{N_C}gS_W\epsilon_1{}^\mu\epsilon_2{}^\nu[(-p_2-p_3-p_4)^\mu\eta^{\nu\rho}+(p_2-p_1)^\rho\eta^{\mu\nu}+(p_1+p_3+p_4)^\nu\eta^{\mu\rho}]$$
$$\times\left[\frac{(1-\xi_A)(-p_3-p_4)^\rho(p_3+p_4)^\sigma}{s^2}+\frac{\eta^{\rho\sigma}}{s}\right]\left[(\bar{u_3}^{\lambda_3}(p_3,M_t)).\left(-\frac{2}{3}igS_W\bar{\gamma}^\sigma.P_R-\frac{2}{3}igS_W\bar{\gamma}^\sigma.P_L\right).\left(v_4^{\lambda_4}(p_4,M_t)\right)\right], \quad \text{(C2)}$$

$$\mathcal{A}_{Z,s} = i\sqrt{N_C}gC_W\epsilon_1{}^\mu\epsilon_2{}^\nu[(-p_2-p_3-p_4)^\mu\eta^{\nu\rho}+(p_2-p_1)^\rho\eta^{\mu\nu}+(p_1+p_3+p_4)^\nu\eta^{\mu\rho}]$$
$$\times\left[\frac{\eta^{\rho\sigma}}{(p_3+p_4)^2-M_Z^2}+\frac{(-p_3-p_4)^\rho(p_3+p_4)^\sigma(1-\xi_Z)}{((p_3+p_4)^2-M_Z^2)((p_3+p_4)^2-M_Z^2\xi_Z)}\right]$$
$$\times\left[(\bar{u_3}^{\lambda_3}(p_3,M_t)).\left(\frac{ig\left(\frac{1}{2}-\frac{2S_W^2}{3}\right)\bar{\gamma}^\sigma.P_L}{C_W}-\frac{2igS_W^2\bar{\gamma}^\sigma.P_R}{3C_W}\right).(v_4^{\lambda_4}(p_4,M_t))\right], \quad \text{(C3)}$$

$$\mathcal{A}_{Z,s} = i\sqrt{N_C} g C_W \epsilon_1{}^{\mu}\epsilon_2{}^{\nu}[(-p_2-p_3-p_4)^{\mu}\eta^{\nu\rho} + (p_2-p_1)^{\rho}\eta^{\mu\nu} + (p_1+p_3+p_4)^{\nu}\eta^{\mu\rho}] \times \left[\frac{\eta^{\rho\sigma}}{(p_3+p_4)^2 - M_Z^2} + \frac{(-p_3-p_4)^{\rho}(p_3+p_4)^{\sigma}(1-\xi_Z)}{((p_3+p_4)^2 - M_Z^2)((p_3+p_4)^2 - M_Z^2\xi_Z)}\right] \times \left[(\bar{u_3}^{\lambda_3}(p_3, M_t)).\left(\frac{ig\left(\frac{1}{2} - \frac{2S_W^2}{3}\right)\bar{\gamma}^{\sigma}.P_L}{C_W} - \frac{2igS_W^2\bar{\gamma}^{\sigma}.P_R}{3C_W}\right).(v_4^{\lambda_4}(p_4, M_t))\right], \tag{C4}$$

$$\mathcal{A}_{b,t} = -\frac{\sqrt{N_c}\epsilon_1{}^{\mu}\epsilon_2{}^{\nu}}{(p_4-p_2)^2 - M_b^2}(\bar{u_3}^{\lambda_3}(p_3, M_t)).\frac{ig\bar{\gamma}^{\mu}.P_L}{\sqrt{2}}.(\bar{\gamma}\cdot(\bar{p}_2 - \bar{p}_4) + M_b).\frac{ig\bar{\gamma}^{\nu}.P_L}{\sqrt{2}}.(v_4^{\lambda_4}(p_4, M_t)). \tag{C5}$$

b. Polarized amplitudes

We have checked these amplitudes via the unitarity relation, finding an agreement with the imaginary part of top-quark loops $\mathcal{A}(W^+W^- \to W^+W^-)$ given in Ref. [21] when we do not consider the exchange of Z or γ bosons. We provide the polarized amplitudes $\mathcal{A}(W_L^+W_L^- \to t(\lambda_3)\bar{t}(\lambda_4)) = Q^{\lambda_3\lambda_4}$, with definite helicities λ_3 and λ_4 for $N_C = 3$:

$$Q^{++} = \frac{g^2 M_t}{16\sqrt{3}M_W^2}\left[\frac{12ac_1\sqrt{s}\beta_t(s-2M_W^2)}{M_H^2 - s} + \frac{3(4\sqrt{s}xM_W^2\beta_W + \sqrt{s}\beta_t(s\beta_W^2 - s(2x^2-1)))}{M_b^2 - t} - \frac{32S_W^2 x\beta_W(2M_W^2+s)}{\sqrt{s}} + \frac{4\sqrt{s}(8S_W^2-3)x\beta_W(2M_W^2+s)}{s-M_Z^2}\right], \tag{C6}$$

$$Q^{--} = -Q^{++}, \tag{C7}$$

$$Q^{+-} = \frac{g^2\sqrt{1-x^2}e^{-i\phi}}{16\sqrt{3}M_W^2}\left[-\frac{3s(\beta_t-1)(s\beta_t(\beta_W+x) - 2M_W^2\beta_W)}{t-M_b^2} + \frac{2s\beta_W(2M_W^2+s)(8S_W^2+3\beta_t-3)}{s-M_Z^2} - 16S_W^2\beta_W(2M_W^2+s)\right], \tag{C8}$$

$$Q^{-+} = \frac{g^2\sqrt{1-x^2}e^{i\phi}}{16\sqrt{3}M_W^2}\left[\frac{3s(\beta_t+1)(s\beta_t(x-\beta_W) - 2M_W^2\beta_W)}{t-M_b^2} + \frac{2s\beta_W(2M_W^2+s)(8S_W^2-3\beta_t-3)}{s-M_Z^2} - 16S_W^2\beta_W(2M_W^2+s)\right]. \tag{C9}$$

2. $\mathcal{A}(W^+(p_1,\epsilon_1^L)W^-(p_2,\epsilon_2^L) \to b(p_3,\lambda_3)\bar{b}(p_4,\lambda_4))$

a. Polarized amplitudes

Since the top and bottom quark form a doublet with the same weak hypercharge, we can relate the amplitudes of the last subsection with the amplitudes $\mathcal{A}(W_L^+W_L^- \to b(\lambda_3)\bar{b}(\lambda_4)) = Q'^{\lambda_3\lambda_4}$ for $b\bar{b}$ scattering, where λ and λ' are the polarization of particle 3 and 4. Then, the amplitude $Q'^{\lambda_3\lambda_4}$ is obtained by applying the following substitutions: $S_W \to S_W/\sqrt{2}$, $\beta_t \leftrightarrow \beta_b$, $M_t \leftrightarrow M_b$, $u \leftrightarrow t$, and $\cos\theta \to -\cos\theta$ on the amplitudes $Q^{\lambda_3\lambda_4}$.

$$Q'^{++} = Q^{++} \qquad (S_W \to S_W/\sqrt{2}, \beta_t \leftrightarrow \beta_b, M_t \leftrightarrow M_b, u \leftrightarrow t, \text{and } \cos\theta \to -\cos\theta), \tag{C10}$$

$$Q'^{+-} = -Q^{+-} \qquad (S_W \to S_W/\sqrt{2}, \beta_t \leftrightarrow \beta_b, M_t \leftrightarrow M_b, u \leftrightarrow t, \text{and } \cos\theta \to -\cos\theta), \tag{C11}$$

$$Q'^{-+} = -Q^{-+} \qquad (S_W \to S_W/\sqrt{2}, \beta_t \leftrightarrow \beta_b, M_t \leftrightarrow M_b, u \leftrightarrow t, \text{and } \cos\theta \to -\cos\theta), \tag{C12}$$

$$Q'^{--} = Q^{--} \qquad (S_W \to S_W/\sqrt{2}, \beta_t \leftrightarrow \beta_b, M_t \leftrightarrow M_b, u \leftrightarrow t, \text{and } \cos\theta \to -\cos\theta). \tag{C13}$$

3. $\mathcal{A}((W^+(p_1,\epsilon_1^L)W^-(p_2,\epsilon_2^L) \to W^+(p_3,\epsilon_3^a)W^-(p_4,\epsilon_4^b))$

a. Amplitudes in terms of the polarization

$$\mathcal{A}_{\text{contact}} = -i\epsilon_1{}^{\mu}\epsilon_2{}^{\nu}\epsilon_3{}^{*\rho}\epsilon_4{}^{*\sigma}(2ig^2\eta^{\mu\sigma}\eta^{\nu\rho} - ig^2\eta^{\mu\rho}\eta^{\nu\sigma} - ig^2\eta^{\mu\nu}\eta^{\rho\sigma}), \tag{C14}$$

$$\mathcal{A}_{H,s} = -a^2\frac{g^2M_W^2\epsilon_1{}^{\mu}\epsilon_2{}^{\nu}\epsilon_3{}^{*\rho}\epsilon_4{}^{*\sigma}\eta^{\mu\nu}\eta^{\rho\sigma}}{(p_3+p_4)^2 - M_H^2}, \tag{C15}$$

$$\begin{aligned} A_{\gamma,s} = &-g^2S_W^2\epsilon_1{}^{\mu}\epsilon_2{}^{\nu}\epsilon_3{}^{*\rho}\epsilon_4{}^{*\sigma}[(p_3-p_4)^{\gamma}\eta^{\rho\sigma} + (-2p_3-p_4)^{\sigma}\eta^{\gamma\rho} + (p_3+2p_4)^{\rho}\eta^{\gamma\sigma}] \\ &\times[(p_2-p_1)^{\delta}\eta^{\mu\nu} + (p_1+p_3+p_4)^{\nu}\eta^{\delta\mu} + (-p_2-p_3-p_4)^{\mu}\eta^{\delta\nu}] \\ &\times\left[\frac{(1-\xi_A)(p_3+p_4)^{\gamma}(-p_3-p_4)^{\delta}}{s^2} + \frac{1}{(p_3+p_4)^2}\eta^{\gamma\delta}\right], \end{aligned} \tag{C16}$$

$$\begin{aligned} \mathcal{A}_{Z,s} = &-C_W^2g^2\epsilon_1{}^{\mu}\epsilon_2{}^{\nu}\epsilon_3{}^{*\rho}\epsilon_4{}^{*\sigma}[(p_3-p_4)^{\gamma}\eta^{\rho\sigma} + (-2p_3-p_4)^{\sigma}\eta^{\gamma\rho} + (p_3+2p_4)^{\rho}\eta^{\gamma\sigma}][(p_2-p_1)^{\delta}\eta^{\mu\nu} \\ &+ (p_1+p_3+p_4)^{\nu}\eta^{\delta\mu} + (-p_2-p_3-p_4)^{\mu}\eta^{\delta\nu}] \\ &\times\left[\frac{\eta^{\gamma\delta}}{(p_3+p_4)^2 - M_Z^2} + \frac{(p_3+p_4)^{\gamma}(-p_3-p_4)^{\delta}(1-\xi_Z)}{((p_3+p_4)^2 - M_Z^2)((p_3+p_4)^2 - M_Z^2\xi_Z)}\right], \end{aligned} \tag{C17}$$

$$\mathcal{A}_{H,t} = -a^2\frac{g^2M_W^2\epsilon_1{}^{\mu}\epsilon_2{}^{\nu}\epsilon_3{}^{*\rho}\epsilon_4{}^{*\sigma}\eta^{\mu\rho}\eta^{\nu\sigma}}{(p_4-p_2)^2 - M_H^2}, \tag{C18}$$

$$\begin{aligned} \mathcal{A}_{\gamma,t} = &-g^2S_W^2\epsilon_1{}^{\mu}\epsilon_2{}^{\nu}\epsilon_3{}^{*\rho}\epsilon_4{}^{*\sigma}[(-p_2-p_4)^{\gamma}\eta^{\nu\sigma} + (2p_2-p_4)^{\sigma}\eta^{\gamma\nu} + (2p_4-p_2)^{\nu}\eta^{\gamma\sigma}] \\ &\times[(-p_1-p_3)^{\delta}\eta^{\mu\rho} + (p_1-p_2+p_4)^{\rho}\eta^{\delta\mu} + (p_2+p_3-p_4)^{\mu}\eta^{\delta\rho}] \\ &\times\left[\left(\frac{1}{(p_4-p_2)^2}\right)^2(1-\xi_A)(p_4-p_2)^{\gamma}(p_2-p_4)^{\delta} + \frac{1}{(p_4-p_2)^2}\eta^{\gamma\delta}\right], \end{aligned} \tag{C19}$$

$$\begin{aligned} \mathcal{A}_{Z,t} = &-C_W^2g^2\epsilon_1{}^{\mu}\epsilon_2{}^{\nu}\epsilon_3{}^{*\rho}\epsilon_4{}^{*\sigma}[(-p_2-p_4)^{\gamma}\eta^{\nu\sigma} + (2p_2-p_4)^{\sigma}\eta^{\gamma\nu} + (2p_4-p_2)^{\nu}\eta^{\gamma\sigma}] \\ &\times[(-p_1-p_3)^{\delta}\eta^{\mu\rho} + (p_1-p_2+p_4)^{\rho}\eta^{\delta\mu} + (p_2+p_3-p_4)^{\mu}\eta^{\delta\rho}] \\ &\times\left[\frac{\eta^{\gamma\delta}}{(p_4-p_2)^2 - M_Z^2} + \frac{(p_4-p_2)^{\gamma}(p_2-p_4)^{\delta}(1-\xi_Z)}{((p_4-p_2)^2 - M_Z^2)((p_4-p_2)^2 - M_Z^2\xi_Z)}\right]. \end{aligned} \tag{C20}$$

b. Polarized amplitudes

We will label the nine polarized amplitudes with $\mathcal{A}_{\epsilon_3\epsilon_4}$, where ϵ_3 and ϵ_4 refer to the polarization of particle 3 and 4, respectively. We have checked the $\mathcal{A}_{LL} \to \mathcal{A}_{LL}$ amplitude with Ref. [22]. We have only four independent amplitudes; the other four can be found through the relations $\mathcal{A}_{NN} = \mathcal{A}_{PP}$, $\mathcal{A}_{NP} = \mathcal{A}_{PN}$, and $\mathcal{A}_{PL} = \mathcal{A}_{NL} = -\mathcal{A}_{LP} = -\mathcal{A}_{NP}$:

$$\begin{aligned} \mathcal{A}_{LL} = &\frac{a^2g^2(4M_W^2 + s(x-1))^2}{8M_W^2(2M_H^2 - s(x-1)\beta_W^2)} + \frac{a^2g^2(s-2M_W^2)^2}{4M_W^2(M_H^2-s)} \\ &+ \frac{g^2C_W^2(-4s^2(x-1)(x(x+10)-3)M_W^2 + 16s(x(10x-7)+1)M_W^4 - 64(x+1)M_W^6 + s^3(x-1)^2(x+3))}{16M_W^4(4(x-1)M_W^2 + 2M_Z^2 - sx + s)} \\ &- \frac{g^2sxC_W^2\beta_W^2(2M_W^2+s)^2}{4M_W^4(s-M_Z^2)} \\ &- \frac{g^2S_W^2(-4s^2(x-1)(x(x+10)-3)M_W^2 + 16s(x(10x-7)+1)M_W^4 - 64(x+1)M_W^6 + s^3(x-1)^2(x+3))}{16s(x-1)M_W^4\beta_W^2} \\ &- \frac{g^2xS_W^2\beta_W^2(2M_W^2+s)^2}{4M_W^4} + \frac{g^2s((8-24x)M_W^2 + s(x(x+6)-3))}{16M_W^4}, \end{aligned} \tag{C21}$$

$$\mathcal{A}_{PP} = \frac{a^2 g^2 s(x^2-1)}{4(2M_H^2 - s(x-1)\beta_W^2)} - \frac{a^2 g^2 (s-2M_W^2)}{2(M_H^2 - s)} + \frac{g^2(x-1)C_W^2(-4s(x-3)(x-1)M_W^2 + 32(x+1)M_W^4 + s^2(x-3)(x-1))}{8M_W^2(4(x-1)M_W^2 + 2M_Z^2 - sx + s)} - \frac{g^2 sx C_W^2 \beta_W^2 (2M_W^2 + s)}{2M_W^2(s - M_Z^2)} + \frac{g^2 S_W^2(-4s(x-3)(x-1)M_W^2 + 32(x+1)M_W^4 + s^2(x-3)(x-1))}{32M_W^4 - 8sM_W^2} - \frac{g^2 x S_W^2 (s-4M_W^2)(2M_W^2+s)}{2sM_W^2} + \frac{g^2(s(x^2+3) - 8M_W^2)}{8M_W^2}, \tag{C22}$$

$$\mathcal{A}_{PN} = \frac{a^2 g^2 s(x^2-1)}{4(2M_H^2 - s(x-1)\beta_W^2)} + \frac{g^2(x^2-1)C_W^2(-4s(x-1)M_W^2 + 32M_W^4 + s^2(x-1))}{8M_W^2(4(x-1)M_W^2 + 2M_Z^2 - sx + s)} + \frac{g^2(x+1)S_W^2(-4s(x-1)M_W^2 + 32M_W^4 + s^2(x-1))}{32M_W^4 - 8sM_W^2} + \frac{g^2 s(x^2-1)}{8M_W^2}, \tag{C23}$$

$$\mathcal{A}_{LP} = \frac{a^2 g^2 \sqrt{s - sx^2}(4M_W^2 + s(x-1))}{4\sqrt{2}M_W(2M_H^2 - s(x-1)\beta_W^2)} + \frac{g^2 C_W^2 \sqrt{s-sx^2}(-4s(x^2+x-2)M_W^2 + 16(5x-3)M_W^4 + s^2(x-1)^2)}{8\sqrt{2}M_W^3(4(x-1)M_W^2 + 2M_Z^2 - sx + s)} - \frac{g^2 C_W^2 \sqrt{s-sx^2}(s-4M_W^2)(2M_W^2+s)}{2\sqrt{2}M_W^3(s-M_Z^2)} - \frac{g^2\sqrt{s-sx^2}S_W^2(-4s(x^2+x-2)M_W^2 + 16(5x-3)M_W^4 + s^2(x-1)^2)}{8\sqrt{2}s(x-1)M_W^3\beta_W^2} - \frac{g^2 s\sqrt{\frac{2-2x^2}{s}}S_W^2\beta_W^2(2M_W^2+s)}{4M_W^3} + \frac{g^2\sqrt{s-sx^2}(s(x+3) - 12M_W^2)}{8\sqrt{2}M_W^3}. \tag{C24}$$

4. $\mathcal{A}(W^+(p_1,\epsilon_1^L)W^-(p_2,\epsilon_2^L) \to Z(p_3,\epsilon_3^a)Z(p_4,\epsilon_4^b))$

a. Amplitudes in terms of the polarization

$$\mathcal{A}_{\text{contact}} = -i\epsilon_1{}^\mu \epsilon_2{}^\nu \epsilon_3{}^{*\rho}\epsilon_4{}^{*\sigma}(iC_W^2 g^2 \eta^{\mu\sigma}\eta^{\nu\rho} + iC_W^2 g^2 \eta^{\mu\rho}\eta^{\nu\sigma} - 2iC_W^2 g^2 \eta^{\mu\nu}\eta^{\rho\sigma}), \tag{C25}$$

$$\mathcal{A}_{H,s} = -a^2 \frac{g^2 M_W^2 \epsilon_1{}^\mu \epsilon_2{}^\nu \epsilon_3{}^{*\rho}\epsilon_4{}^{*\sigma}\eta^{\mu\nu}\eta^{\rho\sigma}}{C_W^2((p_3+p_4)^2 - M_H^2)}, \tag{C26}$$

$$\mathcal{A}_{\pi,t} = -\frac{g^2 S_W^4 M_W^2 \epsilon_1{}^\mu \epsilon_2{}^\nu \epsilon_3{}^{*\rho}\epsilon_4{}^{*\sigma}\eta^{\mu\rho}\eta^{\nu\sigma}}{C_W^2((p_4-p_2)^2 - M_W^2\xi_W)}, \tag{C27}$$

$$\mathcal{A}_{W,t} = -C_W^2 g^2 \epsilon_1{}^\mu \epsilon_2{}^\nu \epsilon_3{}^{*\rho}\epsilon_4{}^{*\sigma}[(-p_2-p_4)^\gamma \eta^{\nu\sigma} + (2p_2-p_4)^\sigma \eta^{\gamma\nu} + (2p_4-p_2)^\nu \eta^{\gamma\sigma}] \times [(-p_1-p_3)^\delta \eta^{\mu\rho} + (p_1-p_2+p_4)^\rho \eta^{\delta\mu} + (p_2+p_3-p_4)^\mu \eta^{\delta\rho}] \times \left[\frac{\eta^{\gamma\delta}}{(p_4-p_2)^2 - M_W^2} + \frac{(p_4-p_2)^\gamma (p_2-p_4)^\delta (1-\xi_W)}{((p_4-p_2)^2 - M_W^2)((p_4-p_2)^2 - M_W^2\xi_W)}\right], \tag{C28}$$

$$\mathcal{A}_{\pi,u} = -\frac{g^2 S_W^4 M_W^2 \epsilon_1{}^\mu \epsilon_2{}^\nu \epsilon_3{}^{*\rho}\epsilon_4{}^{*\sigma}\eta^{\mu\sigma}\eta^{\nu\rho}}{C_W^2((p_3-p_2)^2 - M_W^2\xi_W)}, \tag{C29}$$

$$\mathcal{A}_{W,u} = -C_W^2 g^2 \epsilon_1{}^\mu \epsilon_2{}^\nu \epsilon_3{}^{*\rho}\epsilon_4{}^{*\sigma}[(-p_2-p_3)^\gamma \eta^{\nu\rho} + (2p_2-p_3)^\rho \eta^{\gamma\nu} + (2p_3-p_2)^\nu \eta^{\gamma\rho}] \times [(-p_1-p_4)^\delta \eta^{\mu\sigma} + (p_1-p_2+p_3)^\sigma \eta^{\delta\mu} + (p_2-p_3+p_4)^\mu \eta^{\delta\sigma}] \times \left[\frac{\eta^{\gamma\delta}}{(p_3-p_2)^2 - M_W^2} + \frac{(p_3-p_2)^\gamma (p_2-p_3)^\delta (1-\xi_W)}{((p_3-p_2)^2 - M_W^2)((p_3-p_2)^2 - M_W^2\xi_W)}\right]. \tag{C30}$$

b. Polarized amplitudes

We will label the nine polarized amplitudes with $\mathcal{A}_{\epsilon_3\epsilon_4}$, where ϵ_3 and ϵ_4 refer to the polarization of particle 3 and 4, respectively. We have checked $\mathcal{A}_{LL} \to \mathcal{A}_{LL}$ with Ref. [37]. Just like in the previous case, we have only four independent amplitudes: $\mathcal{A}_{NN} = \mathcal{A}_{PP}$, $\mathcal{A}_{NP} = \mathcal{A}_{PN}$, and $\mathcal{A}_{LP} = \mathcal{A}_{NL} = -\mathcal{A}_{PL} = -\mathcal{A}_{NL}$:

$$\begin{aligned}\mathcal{A}_{LL} = {} & \frac{a^2g^2(2M_W^2 - s)(s - 2M_Z^2)}{4C_W^2M_Z^2(s - M_H^2)} + \frac{g^2sC_W^2(4M_W^2 + 4M_Z^2 + s(x^2 - 3))}{8M_W^2M_Z^2} \\ & + \frac{1}{16M_W^4M_Z^2(2M_Z^2 + sx\beta_W\beta_Z - s)}[-g^2C_W^2(-4M_W^4(4sx^2(s - 6M_Z^2) - 2sM_Z^2 + 24M_Z^4 + s^2) \\ & + 2s^2x^2M_Z^4 + M_W^2(-2s^2(11x^2 + 5)M_Z^2 + 16M_Z^4(2sx^2 + s) + 32M_Z^6 + s^3(x^2 + 3)) \\ & + s\beta_Z(x\beta_W(sM_W^2(24M_Z^2 + s(x^2 - 5)) + 4M_W^4(4M_Z^2 + 3s) - 4sM_Z^4) + 2sM_Z^4\beta_Z) + 32sx^2M_W^6)] \\ & - \frac{1}{16M_W^4M_Z^2(2M_Z^2 - sx\beta_W\beta_Z - s)}[-g^2C_W^2(-4M_W^4(4sx^2(s - 6M_Z^2) - 2sM_Z^2 + 24M_Z^4 + s^2) \\ & + 2s^2x^2M_Z^4 + M_W^2(-2s^2(11x^2 + 5)M_Z^2 + 16M_Z^4(2sx^2 + s) + 32M_Z^6 + s^3(x^2 + 3)) \\ & + s\beta_Z(-x\beta_W(sM_W^2(24M_Z^2 + s(x^2 - 5)) + 4M_W^4(4M_Z^2 + 3s) - 4sM_Z^4) + 2sM_Z^4\beta_Z) + 32sx^2M_W^6)],\end{aligned} \tag{C31}$$

$$\begin{aligned}\mathcal{A}_{PP} = {} & \frac{g^2C_W^2(s(x^2 + 3) - 8M_W^2)}{4M_W^2} - \frac{a^2g^2(s - 2M_W^2)}{2C_W^2(M_H^2 - s)} \\ & + \frac{1}{8M_W^4(2M_Z^2 - s + sx\beta_W\beta_Z)}[-g^2C_W^2(32(x^2 - 1)M_W^6 + 8s(x^2 + 1)M_W^4 + s(2(5x^2 + 3)M_Z^2 \\ & - s(5x^2 + 3) + sx(x^2 + 7)\beta_W\beta_Z)M_W^2 + 2s(x^2 - 1)M_Z^4)],\end{aligned} \tag{C32}$$

$$\begin{aligned}\mathcal{A}_{PN} = {} & \frac{g^2s(x^2 - 1)C_W^2}{4M_W^2} - \frac{g^2(x^2 - 1)C_W^2}{8M_W^4(2M_Z^2 + sx\beta_W\beta_Z - s)}(-sM_W^2(6M_Z^2 - sx\beta_W\beta_Z + s) + 8sM_W^4 + 2sM_Z^4 + 32M_W^6) \\ & + \frac{g^2(x^2 - 1)C_W^2}{8M_W^4(-2M_Z^2 + sx\beta_W\beta_Z + s)}(-sM_W^2(6M_Z^2 + sx\beta_W\beta_Z + s) + 8sM_W^4 + 2sM_Z^4 + 32M_W^6),\end{aligned} \tag{C33}$$

$$\begin{aligned}\mathcal{A}_{LP} = {} & \frac{g^2s^{3/2}x\sqrt{1 - x^2}C_W^2}{4\sqrt{2}M_W^2M_Z} + \frac{1}{8\sqrt{2}M_W^4M_Z(2M_Z^2 + s(x\beta_W\beta_Z - 1))}\Big[-g^2C_W^2\sqrt{s - sx^2}(sM_W^2(\beta_W\beta_Z(6M_Z^2 + sx^2 + s) \\ & - 2x(M_Z^2 + s)) + M_W^4(48xM_Z^2 + 8s\beta_W\beta_Z - 4sx) + 2sM_Z^4(x - \beta_W\beta_Z) + 32xM_W^6)\Big] \\ & + \frac{1}{8\sqrt{2}M_W^4M_Z(-2M_Z^2 + sx\beta_W\beta_Z + s)}\Big[-g^2C_W^2\sqrt{s - sx^2}(sM_W^2(\beta_W\beta_Z(6M_Z^2 + sx^2 + s) \\ & + 2x(M_Z^2 + s)) + 4M_W^4(s(2\beta_W\beta_Z + x) - 12xM_Z^2) - 2sM_Z^4(\beta_W\beta_Z + x) - 32xM_W^6)\Big].\end{aligned} \tag{C34}$$

5. $\mathcal{A}(W^+(p_1,\epsilon_1^L)W^-(p_2,\epsilon_2^L) \to \gamma(p_3,\epsilon_3^a)\gamma(p_4,\epsilon_4^b))$

a. Amplitudes in terms of the polarization

$$\mathcal{A}_{\text{contact}} = -ie\epsilon_1{}^\mu\epsilon_2{}^\nu\epsilon_3{}^{*\rho}\epsilon_4{}^{*\sigma}S_W^2(ig^2\eta^{\mu\sigma}\eta^{\nu\rho} + ig^2\eta^{\mu\rho}\eta^{\nu\sigma} - 2ig^2\eta^{\mu\nu}\eta^{\rho\sigma}), \tag{C35}$$

$$\mathcal{A}_{\pi,t} = -\frac{g^2S_W^2M_W^2\epsilon_1{}^\mu\epsilon_2{}^\nu\epsilon_3{}^{*\rho}\epsilon_4{}^{*\sigma}\eta^{\mu\rho}\eta^{\nu\sigma}}{(p_4 - p_2)^2 - M_W^2\xi_W}, \tag{C36}$$

$$\mathcal{A}_{W,t} = -g^2 S_W^2 \epsilon_1{}^{\mu} \epsilon_2{}^{\nu} \epsilon_3{}^{*\rho} \epsilon_4{}^{*\sigma} [(-p_2 - p_4)^{\gamma} \eta^{\nu\sigma} + (2p_2 - p_4)^{\sigma} \eta^{\gamma\nu} + (2p_4 - p_2)^{\nu} \eta^{\gamma\sigma}] \times [(-p_1 - p_3)^{\delta} \eta^{\mu\rho} + (p_1 - p_2 + p_4)^{\rho} \eta^{\delta\mu} + (p_2 + p_3 - p_4)^{\mu} \eta^{\delta\rho}] \times \left[\frac{\eta^{\gamma\delta}}{(p_4 - p_2)^2 - M_W^2} + \frac{(p_4 - p_2)^{\gamma} (p_2 - p_4)^{\delta} (1 - \xi_W)}{((p_4 - p_2)^2 - M_W^2)((p_4 - p_2)^2 - M_W^2 \xi_W)} \right], \tag{C37}$$

$$\mathcal{A}_{\pi,u} = -\frac{g^2 S_W^2 M_W^2 \epsilon_1{}^{\mu} \epsilon_2{}^{\nu} \epsilon_3{}^{*\rho} \epsilon_4{}^{*\sigma} \eta^{\mu\sigma} \eta^{\nu\rho}}{(p_3 - p_2)^2 - M_W^2 \xi_W}, \tag{C38}$$

$$\mathcal{A}_{W,u} = -g^2 S_W^2 \epsilon_1{}^{\mu} \epsilon_2{}^{\nu} \epsilon_3{}^{*\rho} \epsilon_4{}^{*\sigma} [(-p_2 - p_3)^{\gamma} \eta^{\nu\rho} + (2p_2 - p_3)^{\rho} \eta^{\gamma\nu} + (2p_3 - p_2)^{\nu} \eta^{\gamma\rho}] \times [(-p_1 - p_4)^{\delta} \eta^{\mu\sigma} + (p_1 - p_2 + p_3)^{\sigma} \eta^{\delta\mu} + (p_2 - p_3 + p_4)^{\mu} \eta^{\delta\sigma}] \times \left[\frac{\eta^{\gamma\delta}}{(p_3 - p_2)^2 - M_W^2} + \frac{(p_3 - p_2)^{\gamma} (p_2 - p_3)^{\delta} (1 - \xi_W)}{((p_3 - p_2)^2 - M_W^2)((p_3 - p_2)^2 - M_W^2 \xi_W)} \right]. \tag{C39}$$

b. Polarized amplitudes

We have checked the polarized amplitudes with Ref. [38], finding an agreement. We have only two independent amplitudes since $\mathcal{A}_{++} = \mathcal{A}_{--}$ and $\mathcal{A}_{+-} = \mathcal{A}_{-+}$, where $+$ and $-$ refer to the positive and negative polarization, respectively, of the photons:

$$\mathcal{A}_{++} = -\frac{8 g^2 M_W^2 S_W^2}{x^2 (4M_W^2 - s) + s}, \tag{C40}$$

$$\mathcal{A}_{+-} = \frac{2 g^2 (x^2 - 1) S_W^2 (4M_W^2 + s)}{x^2 (4M_W^2 - s) + s}. \tag{C41}$$

6. $\mathcal{A}(W^+(p_1, \epsilon_1^L) W^-(p_2, \epsilon_2^L) \to h(p_3) h(p_4))$

a. Amplitudes

$$\mathcal{A}_{\text{contact}} = \frac{1}{2} b g^2 \epsilon_1{}^{\mu} \epsilon_2{}^{\nu} \eta^{\mu\nu}, \tag{C42}$$

$$\mathcal{A}_{H,s} = \frac{3 g^2 M_H^2 \epsilon_1{}^{\mu} \epsilon_2{}^{\nu} \eta^{\mu\nu}}{2((p_3 + p_4)^2 - M_H^2)} a d_3, \tag{C43}$$

$$\mathcal{A}_{\pi,t} = a^2 \frac{g^2 (-p_2 - p_3 + p_4)^{\mu} (p_2 - 2p_4)^{\nu} \epsilon_1{}^{\mu} \epsilon_2{}^{\nu}}{4((p_4 - p_2)^2 - M_W^2 \xi_W)}, \tag{C44}$$

$$\mathcal{A}_{W,t} = a^2 g^2 M_W^2 \epsilon_1{}^{\mu} \epsilon_2{}^{\nu} \eta^{\mu\rho} \eta^{\nu\sigma} \left[\frac{\eta^{\rho\sigma}}{(p_4 - p_2)^2 - M_W^2} + \frac{(p_2 - p_4)^{\rho} (p_4 - p_2)^{\sigma} (1 - \xi_W)}{((p_4 - p_2)^2 - M_W^2)((p_4 - p_2)^2 - M_W^2 \xi_W)} \right], \tag{C45}$$

$$\mathcal{A}_{\pi,u} = a^2 \frac{g^2 (-p_2 + p_3 - p_4)^{\mu} (p_2 - 2p_3)^{\nu} \epsilon_1{}^{\mu} \epsilon_2{}^{\nu}}{4((p_3 - p_2)^2 - M_W^2 \xi_W)}, \tag{C46}$$

$$\mathcal{A}_{W,u} = a^2 g^2 M_W^2 \epsilon_1{}^{\mu} \epsilon_2{}^{\nu} \eta^{\mu\rho} \eta^{\nu\sigma} \left[\frac{\eta^{\rho\sigma}}{(p_3 - p_2)^2 - M_W^2} + \frac{(p_2 - p_3)^{\rho} (p_3 - p_2)^{\sigma} (1 - \xi_W)}{((p_3 - p_2)^2 - M_W^2)((p_3 - p_2)^2 - M_W^2 \xi_W)} \right]. \tag{C47}$$

We have checked the amplitude with Refs. [27,39]. Since the Higgs boson h is a scalar particle, the only amplitude is

$$\mathcal{A}_{W^+W^-\to hh} = \frac{a^2(s^2(\beta_W - x\beta_H)^2 + 8M_W^2(s-2M_W^2))}{2v^2(2M_H^2 + sx\beta_H\beta_W - s)} - \frac{a^2(s^2(x\beta_H + \beta_W)^2 + 8M_W^2(s-2M_W^2))}{2v^2(-2M_H^2 + sx\beta_H\beta_W + s)} - \frac{3ad_3M_H^2(s-2M_W^2)}{v^2(M_H^2 - s)} + \frac{b(s-2M_W^2)}{v^2}. \tag{C48}$$

7. $\mathcal{A}(W^+(p_1,\epsilon_1^L)W^-(p_2,\epsilon_2^L) \to Z(p_3,\epsilon_3^a)h(p_4))$

a. Amplitudes in terms of the polarization

$$\mathcal{A}_{Z,s} = a\frac{g^2M_W}{C_W}\epsilon_1{}^\mu\epsilon_2{}^\nu\epsilon_3{}^{*\rho}\eta^{\delta\rho}[(-p_2-p_3-p_4)^\mu\eta^{\nu\sigma} + (p_2-p_1)^\sigma\eta^{\mu\nu} + (p_1+p_3+p_4)^\nu\eta^{\mu\sigma}] \times \left[\frac{\eta^{\delta\sigma}}{(p_3+p_4)^2 - M_Z^2} + \frac{(p_3+p_4)^\delta(-p_3-p_4)^\sigma(1-\xi_Z)}{((p_3+p_4)^2 - M_Z^2)((p_3+p_4)^2 - M_Z^2\xi_Z)}\right], \tag{C49}$$

$$\mathcal{A}_{\pi,t} = -a\frac{g^2S_W^2M_W(p_2-2p_4)^\nu\epsilon_1{}^\mu\epsilon_2{}^\nu\epsilon_3{}^{*\rho}\eta^{\mu\rho}}{2C_W((p_4-p_2)^2 - M_W^2\xi_W)}, \tag{C50}$$

$$\mathcal{A}_{W,t} = -aC_Wg^2M_W\epsilon_1{}^\mu\epsilon_2{}^\nu\epsilon_3{}^{*\rho}\eta^{\delta\nu}[(p_2+p_3-p_4)^\mu\eta^{\rho\sigma} + (-p_1-p_3)^\sigma\eta^{\mu\rho} + (p_1-p_2+p_4)^\rho\eta^{\mu\sigma}] \times \left[\frac{\eta^{\delta\sigma}}{(p_4-p_2)^2 - M_W^2} + \frac{(p_4-p_2)^\delta(p_2-p_4)^\sigma(1-\xi_W)}{((p_4-p_2)^2 - M_W^2)((p_4-p_2)^2 - M_W^2\xi_W)}\right], \tag{C51}$$

$$\mathcal{A}_{\pi,u} = a\frac{g^2S_W^2M_W(-p_2+p_3-p_4)^\mu\epsilon_1{}^\mu\epsilon_2{}^\nu\epsilon_3{}^{*\rho}\eta^{\nu\rho}}{2C_W((p_3-p_2)^2 - M_W^2\xi_W)}, \tag{C52}$$

$$\mathcal{A}_{W,u} = aC_Wg^2M_W\epsilon_1{}^\mu\epsilon_2{}^\nu\epsilon_3{}^{*\rho}\eta^{\mu\sigma}[(-p_2-p_3)^\delta\eta^{\nu\rho} + (2p_2-p_3)^\rho\eta^{\delta\nu} + (2p_3-p_2)^\nu\eta^{\delta\rho}] \times \left[\frac{\eta^{\delta\sigma}}{(p_3-p_2)^2 - M_W^2} + \frac{(p_3-p_2)^\delta(p_2-p_3)^\sigma(1-\xi_W)}{((p_3-p_2)^2 - M_W^2)((p_3-p_2)^2 - M_W^2\xi_W)}\right]. \tag{C53}$$

b. Polarized amplitudes

We will label the polarized amplitude with $\mathcal{A}_{\epsilon_3}$, where ϵ_3 refers to the polarization of the Z boson. We have only two independent amplitudes, since $\mathcal{A}_P = \mathcal{A}_N$:

$$\begin{aligned}\mathcal{A}_L =& \frac{ag^2x\beta_W(2M_W^2+s)(-M_H^2+M_Z^2+s)}{4C_WM_WM_Z(M_Z^2-s)} \\ &+ \frac{-ag^2C_W}{8sM_W^3M_Z(M_H^2+M_Z^2-s)(x\beta_W-1)} \times [(M_H^2+M_Z^2-s)(-8sM_W^4 + 4(-M_Z^4+sM_Z^2+s^2)M_W^2 \\ &+ M_H^2(4M_W^2 + s(x^2-1))M_Z^2 - sM_Z^2((M_Z^2+s)x^2 - M_Z^2+s)) + 2sx(-4(M_Z^2+s)M_W^4 \\ &+ 2s(s-3M_Z^2)M_W^2 + sM_Z^2(M_Z^2-s) + M_H^2(4M_W^4 - 2sM_W^2 + sM_Z^2))\beta_W)] \\ &- \frac{-ag^2C_W}{8sM_W^3M_Z(M_H^2+M_Z^2-s)(-x\beta_W-1)} \times [(M_H^2+M_Z^2-s)(-8sM_W^4 + 4(-M_Z^4+sM_Z^2+s^2)M_W^2 \\ &+ M_H^2(4M_W^2 + s(x^2-1))M_Z^2 - sM_Z^2((M_Z^2+s)x^2 - M_Z^2+s)) - 2sx(-4(M_Z^2+s)M_W^4 \\ &+ 2s(s-3M_Z^2)M_W^2 + sM_Z^2(M_Z^2-s) + M_H^2(4M_W^4 - 2sM_W^2 + sM_Z^2))\beta_W)],\end{aligned} \tag{C54}$$

$$\mathcal{A}_P = \frac{ag^2(2M_W^2+s)\sqrt{-s(x^2-1)\beta_W^2}}{2\sqrt{2}C_W M_W(s-M_Z^2)} + \frac{a}{4\sqrt{2}M_W^3(-M_H^2-M_Z^2+s)(x\beta_W-1)}\Big[g^2\sqrt{s(1-x^2)}C_W(x(M_H^2+M_Z^2-s)M_Z^2 + (8M_W^4-4M_H^2M_W^2-M_Z^4+(M_H^2+4M_W^2+s)M_Z^2)\beta_W)\Big] + \frac{a}{4\sqrt{2}M_W^3(-M_H^2-M_Z^2+s)(x\beta_W+1)} \times \Big[g^2\sqrt{s(1-x^2)}C_W((x+\beta_W)M_Z^4-((\beta_W-x)M_H^2+sx+(4M_W^2+s)\beta_W)M_Z^2+4M_W^2(M_H^2-2M_W^2)\beta_W)\Big]. \quad \text{(C55)}$$

8. $\mathcal{A}(W^+(p_1,\epsilon_1^L)W^-(p_2,\epsilon_2^L)\to\gamma(p_3,\epsilon_3^a)h(p_4))$

a. Amplitudes in terms of the polarization

$$A_{\pi,t} = -a\frac{g^2 S_W M_W (p_2-2p_4)^\nu \epsilon_1{}^\mu \epsilon_2{}^\nu \epsilon_3{}^{*\rho}\eta^{\mu\rho}}{2((p_4-p_2)^2-M_W^2\xi_W)}, \quad \text{(C56)}$$

$$\mathcal{A}_{W,t} = ag^2 S_W M_W \epsilon_1{}^\mu \epsilon_2{}^\nu \epsilon_3{}^{*\rho}\eta^{\delta\nu}[(p_2+p_3-p_4)^\mu\eta^{\rho\sigma}+(-p_1-p_3)^\sigma\eta^{\mu\rho}+(p_1-p_2+p_4)^\rho\eta^{\mu\sigma}] \times\left[\frac{\eta^{\delta\sigma}}{(p_4-p_2)^2-M_W^2}+\frac{(p_4-p_2)^\delta(p_2-p_4)^\sigma(1-\xi_W)}{((p_4-p_2)^2-M_W^2)((p_4-p_2)^2-M_W^2\xi_W)}\right], \quad \text{(C57)}$$

$$\mathcal{A}_{\pi,u} = a\frac{g^2 S_W M_W (-p_2+p_3-p_4)^\mu \epsilon_1{}^\mu \epsilon_2{}^\nu \epsilon_3{}^{*\rho}\eta^{\nu\rho}}{2((p_3-p_2)^2-M_W^2\xi_W)}, \quad \text{(C58)}$$

$$\mathcal{A}_{W,u} = -ag^2 S_W M_W \epsilon_1{}^\mu \epsilon_2{}^\nu \epsilon_3{}^{*\rho}\eta^{\mu\sigma}[(-p_2-p_3)^\delta\eta^{\nu\rho}+(2p_2-p_3)^\rho\eta^{\delta\nu}+(2p_3-p_2)^\nu\eta^{\delta\rho}] \times\left[\frac{\eta^{\delta\sigma}}{(p_3-p_2)^2-M_W^2}+\frac{(p_3-p_2)^\delta(p_2-p_3)^\sigma(1-\xi_W)}{((p_3-p_2)^2-M_W^2)((p_3-p_2)^2-M_W^2\xi_W)}\right]. \quad \text{(C59)}$$

b. Polarized amplitudes

We will label the polarized amplitudes with $\mathcal{A}_{\epsilon_3}$, where ϵ_3 refers to the polarization of the photon. The only independent amplitude is ($\mathcal{A}_+ = \mathcal{A}_-$), where + or − refers to the polarization of the photon:

$$\mathcal{A}_+ = \frac{ag^2\sqrt{s}\sqrt{2-2x^2}S_W\beta_W(M_H^2-2M_W^2)}{M_W(s-M_H^2)(x^2\beta_W^2-1)}.$$

9. $\mathcal{A}(W^+(p_1,\epsilon_1^L)W^-(p_2,\epsilon_2^L)\to\gamma(p_3,\epsilon_3^a)Z(p_4,\epsilon_4))$

a. Amplitude

$$\mathcal{A}_{\text{contact}} = -i\epsilon_1{}^\mu \epsilon_2{}^\nu \epsilon_3{}^{*\rho}\epsilon_4{}^{*\sigma}C_W g^2 S_W(-i\eta^{\mu\sigma}\eta^{\nu\rho}-i\eta^{\mu\rho}\eta^{\nu\sigma}+2i\eta^{\mu\nu}\eta^{\rho\sigma}), \quad \text{(C60)}$$

$$\mathcal{A}_{\pi,t} = -\frac{g^2 S_W^3 M_W^2 \epsilon_1{}^\mu \epsilon_2{}^\nu \epsilon_3{}^{*\rho}\epsilon_4{}^{*\sigma}\eta^{\mu\rho}\eta^{\nu\sigma}}{C_W((p_4-p_2)^2-M_W^2\xi_W)}, \quad \text{(C61)}$$

$$\mathcal{A}_{W,t} = C_W g^2 S_W \epsilon_1{}^\mu \epsilon_2{}^\nu \epsilon_3{}^{*\rho}\epsilon_4{}^{*\sigma}[(-p_2-p_4)^\gamma\eta^{\nu\sigma}+(2p_2-p_4)^\sigma\eta^{\gamma\nu}+(2p_4-p_2)^\nu\eta^{\gamma\sigma}] \times[(-p_1-p_3)^\delta\eta^{\mu\rho}+(p_1-p_2+p_4)^\rho\eta^{\delta\mu}+(p_2+p_3-p_4)^\mu\eta^{\delta\rho}] \times\left[\frac{\eta^{\gamma\delta}}{(p_4-p_2)^2-M_W^2}+\frac{(p_4-p_2)^\gamma(p_2-p_4)^\delta(1-\xi_W)}{((p_4-p_2)^2-M_W^2)((p_4-p_2)^2-M_W^2\xi_W)}\right], \quad \text{(C62)}$$

$$\mathcal{A}_{\pi,u} = -\frac{g^2 S_W^3 M_W^2 \epsilon_1{}^{\mu} \epsilon_2{}^{\nu} \epsilon_3{}^{*\rho} \epsilon_4{}^{*\sigma} \eta^{\mu\sigma} \eta^{\nu\rho}}{C_W((p_3-p_2)^2 - M_W^2 \xi_W)}, \tag{C63}$$

$$\begin{aligned}\mathcal{A}_{W,u} = {} & C_W g^2 S_W \epsilon_1{}^{\mu} \epsilon_2{}^{\nu} \epsilon_3{}^{*\rho} \epsilon_4{}^{*\sigma} [(-p_2-p_3)^{\gamma} \eta^{\nu\rho} + (2p_2-p_3)^{\rho} \eta^{\gamma\nu} + (2p_3-p_2)^{\nu} \eta^{\gamma\rho}] \\ & \times [(-p_1-p_4)^{\delta} \eta^{\mu\sigma} + (p_1-p_2+p_3)^{\sigma} \eta^{\delta\mu} + (p_2-p_3+p_4)^{\mu} \eta^{\delta\sigma}] \\ & \times \left[\frac{\eta^{\gamma\delta}}{(p_3-p_2)^2 - M_W^2} + \frac{(p_3-p_2)^{\gamma}(p_2-p_3)^{\delta}(1-\xi_W)}{((p_3-p_2)^2 - M_W^2)((p_3-p_2)^2 - M_W^2 \xi_W)}\right].\end{aligned} \tag{C64}$$

b. Polarized amplitudes

We will label the polarized amplitudes with $\mathcal{A}_{\epsilon_3\epsilon_4}$, where ϵ_3 and ϵ_4 refer to the polarizations of the photon and the Z boson. We have only three independent amplitudes since $\mathcal{A}_{+L} = \mathcal{A}_{-L}$, $\mathcal{A}_{+P} = \mathcal{A}_{-N}$, and $\mathcal{A}_{+N} = \mathcal{A}_{-P}$:

$$\mathcal{A}_{+L} = \frac{2g^2 x\sqrt{1-x^2} C_W M_Z S_W (-2sM_W^2 + sM_Z^2 - 8M_W^4)}{\sqrt{s} M_W^2 (s - M_Z^2)(x^2 \beta_W^2 - 1)}, \tag{C65}$$

$$\mathcal{A}_{+P} = \frac{g^2 C_W S_W (-8M_W^4 (s - x^2 M_Z^2) + 2M_W^2 M_Z^2 (-2M_Z^2 + sx^2 + s) - s(x^2-1)M_Z^4)}{M_W^2 (M_Z^2 - s)(x^2(4M_W^2 - s) + s)}, \tag{C66}$$

$$\mathcal{A}_{+N} = -\frac{g^2 (x^2-1) C_W S_W (2sM_W^2 - sM_Z^2 + 8M_W^4)}{M_W^2 (M_Z^2 - s)(x^2 \beta_W^2 - 1)}. \tag{C67}$$

APPENDIX D: COMPLETE CONTRIBUTION OF EACH CHANNEL TO THE P-PWAs

In this appendix, we will provide the plots for the cumulative ratios $\chi_i^{J'}$ for the p-PWAs for $g' \neq 0$. For the sake of clarity, in the main text we separated the plots in bosonic cuts, $b\bar{b}$ cuts, and $t\bar{t}$ cuts. Therefore, we did not specify the contributions from each individual channel, as they were very numerous for $g' \neq 0$. The plots must be read in the same way as the PWA cumulative ratios χ_i^J in Sec. IV ($g' = 0$ case): Each line contains the relative cumulative contribution of the past cuts. Hence, the shaded area accounts for the contribution of the same-color curve directly above it.

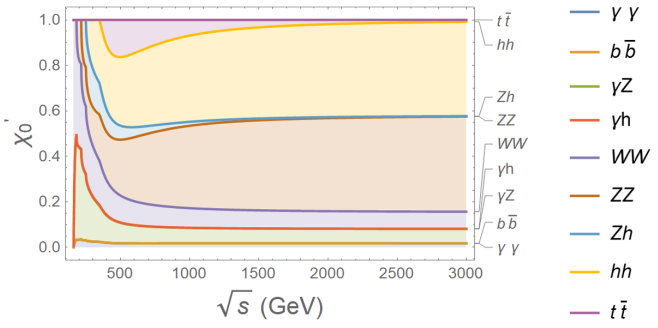

FIG. 34. Ratio for the R_0' p-PWAs at the SM.

Some contributions are difficult to see, because the curves are close to each other and some of them directly overlap. For the $J = 0$ p-PWA, we observe this for the $b\bar{b}$ cut and $\gamma\gamma$ in Figs. 34–36. While the $\gamma\gamma$ contribution (bottom in pale blue) can still be appreciated (barely) between the x axis and the orange curve, the $b\bar{b}$ channel is very suppressed and sits on top of the $\gamma\gamma$, impossible to see because of its negligible contribution. The same occurs for the γh and γZ curves in the mentioned plots, where the γh channel is essentially negligible and its curve sits on top of the γZ one. For the $J = 1$ p-PWA in Figs. 37–39, this time it is the γZ curve which sits on top of the $b\bar{b}$ and cannot be seen as is shown in the figures. The same occurs for the ZZ cut which sits on top of the WW curve in the same plots mentioned.

In general, if the shaded area is not of the same color of the curve immediately above it, a second curve with a negligible contribution sits on top of the first one.

1. $J = 0$ pseudo-PWA: χ_0'

We provide Figs. 34–36 corresponding to the ratios χ_0' for a $|\cos\theta| \leq 0.9$ angular integration for all absorptive cuts explained in explained in Sec. V A.

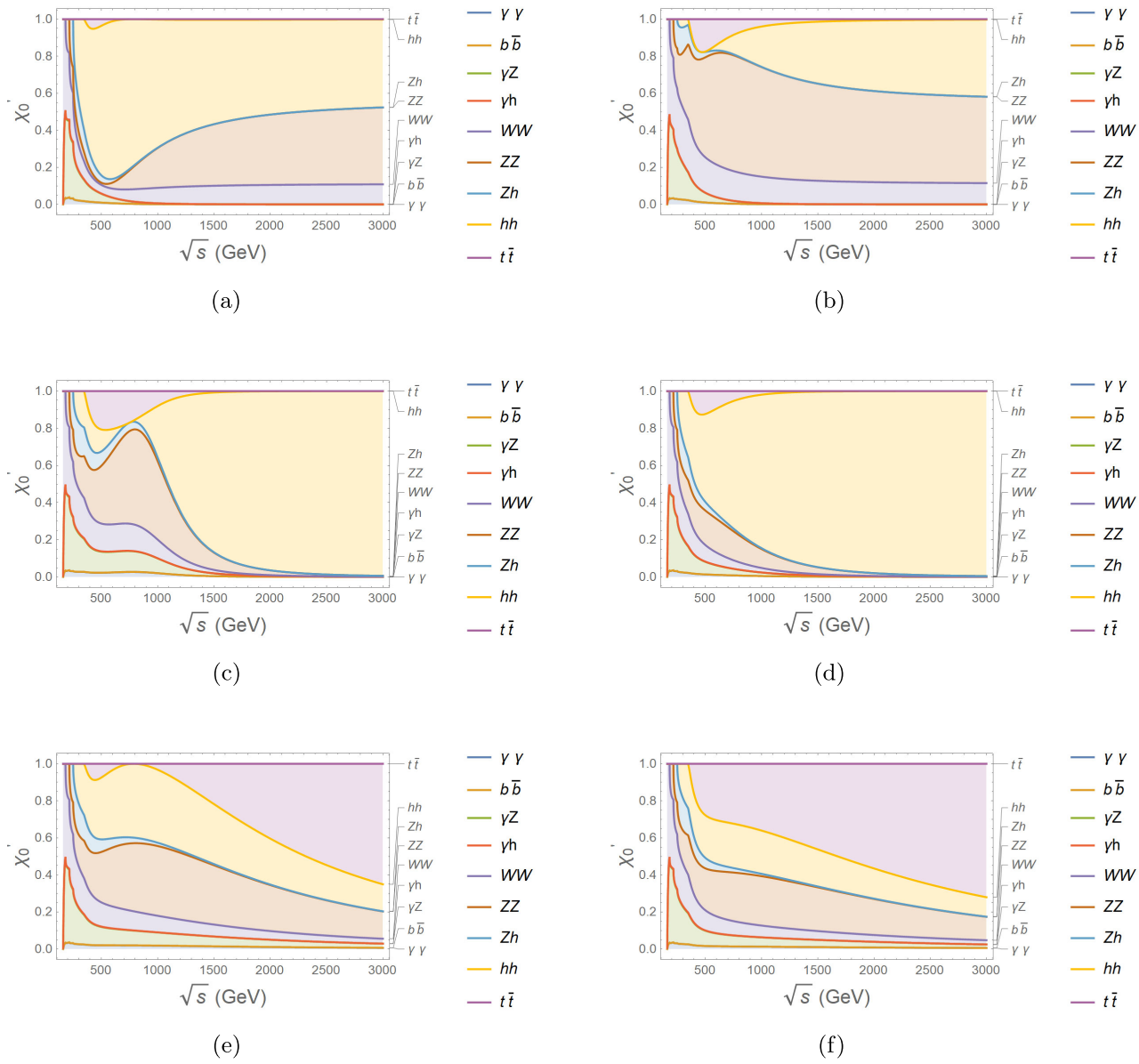

FIG. 35. (a) $J = 0$ p-PWA: contribution of each channel for $a = 1.10$ and $b = c_1 = d_3 = 1$. (b) $J = 0$ p-PWA: contribution of each channel for $a = 0.90$ and $b = c_1 = d_3 = 1$. (c) $J = 0$ p-PWA: contribution of each channel for $b = 1.1$ and $a = d_3 = 1$. (d) $J = 0$ p-PWA: contribution of each channel for $b = 0.90$ and $b = d_3 = 1$. (e) $J = 0$ p-PWA: contribution of each channel for $c_1 = 1.10$ and $a = b = d_3 = 1$. (f) $J = 0$ p-PWA: contribution of each channel for $c_1 = 0.90$ and $a = b = d_3 = 1$.

2. $J = 1$ pseudo-PWA: χ_1'

We provide Figs. 37–39 corresponding to the ratios χ_1' for a $|\cos\theta| = 0.9$ angular integration for all absorptive cuts explained in Sec. V B.

3. $J = 0$ pseudo-PWA: Sensitivity of R_0' to the optimal points

For the case of the $J = 0$ p-PWA R_0', we have plotted the sensitivity to the optimal parameters (a, b, c_1, d_3) in Fig. 40. All notations are analogous to those for R_0 in Fig. 6.

4. $J = 1$ pseudo-PWA: Sensitivity of R_1' to the optimal points

For the case of the $J = 1$ p-PWA R_1', we have plotted the sensitivity to the a parameter in Fig. 41. All notations are analogous to those for R_1 in Fig. 11.

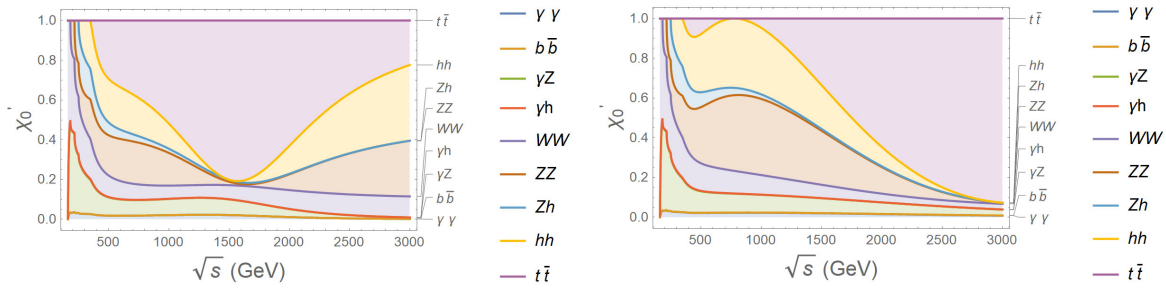

(a) (b)

FIG. 36. (a) $J = 0$ p-PWA: largest fermion-loop contribution of 80% at 1.5 TeV for $a = 1.011$, $b = 1.045$, $c_1 = 0.900$, and $d_3 = 1.094$. (b) $J = 0$ p-PWA: largest fermion-loop contribution of 93% at 3 TeV happens for $a = 1.003$, $b = 1.011$, $c_1 = 1.100$, and $d_3 = 1.100$.

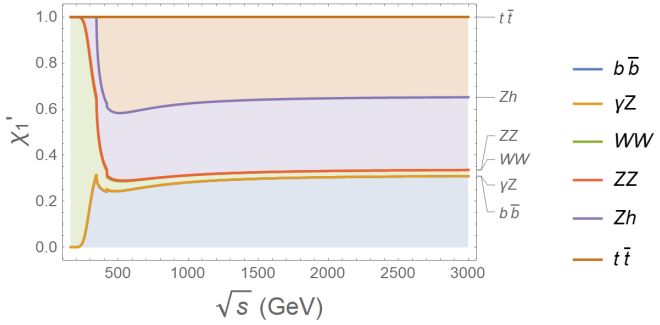

FIG. 37. Ratio for the R_1' p-PWA at the SM.

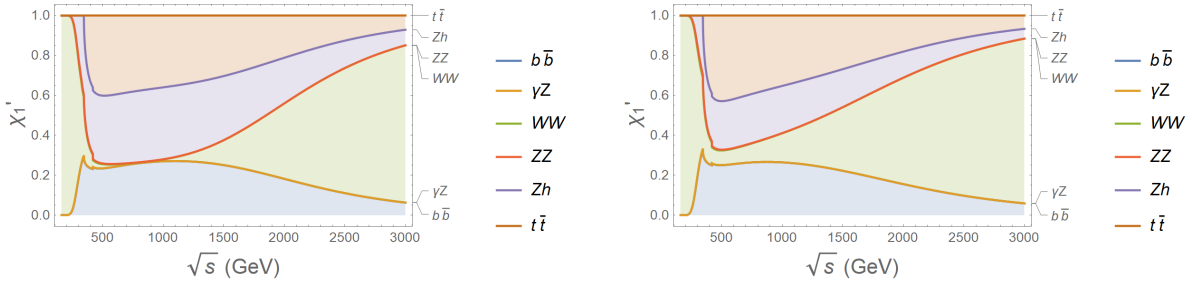

(a) (b)

FIG. 38. (a) $J = 1$ p-PWA: contribution of each channel for $a = 1.10$. (b) $J = 1$ p-PWA: contribution of each channel for $a = 0.90$.

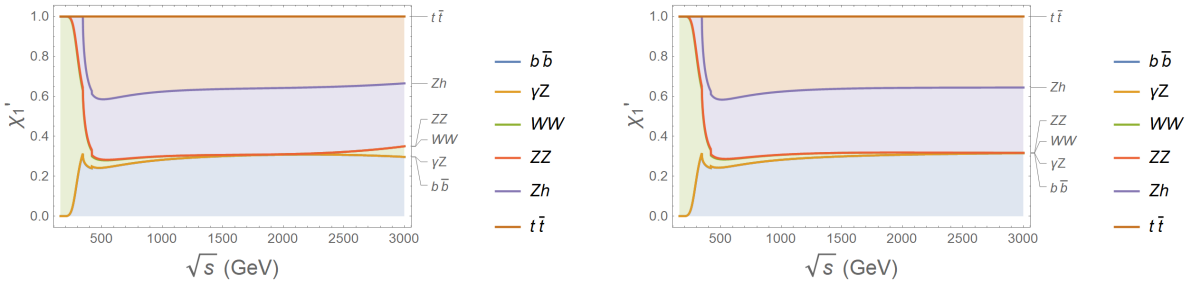

(a) (b)

FIG. 39. (a) $J = 1$ p-PWA: largest fermion-loop contribution of 75% at 1.5 TeV for $a = 1.019$. (b) $J = 1$ p-PWA: largest fermion-loop contribution of 76% at 3 TeV for $a = 1.007$.

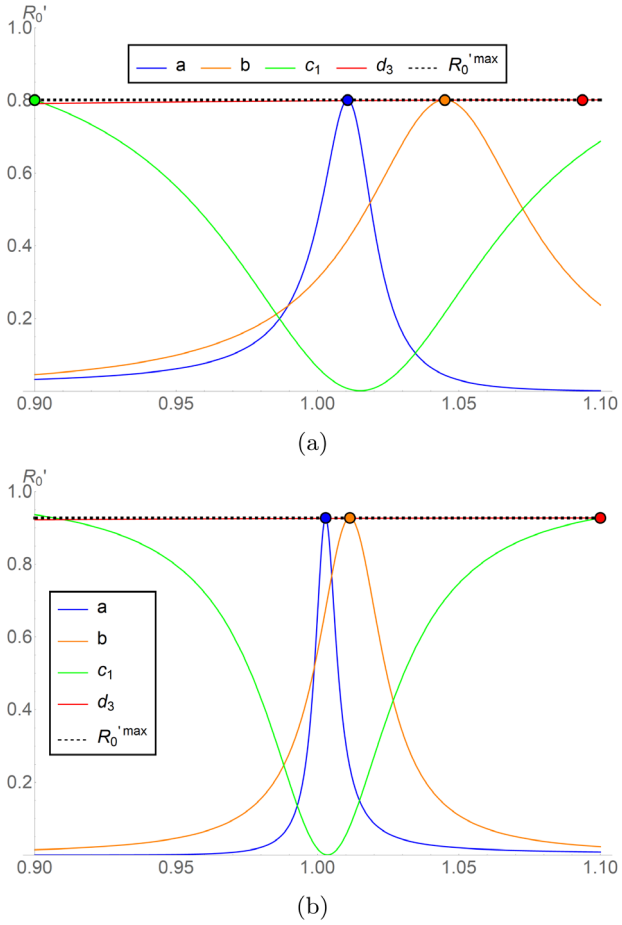

(a)

(b)

FIG. 40. Sensitivity of R_0' to each parameter when the rest are set to the highest correction value at $\sqrt{s} = 1.5$ (top) and $\sqrt{3}$ (bottom) TeV.

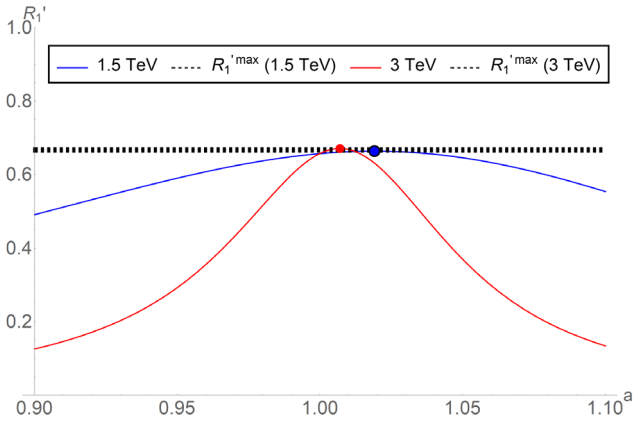

FIG. 41. Sensitivity of R_1' to the a parameter for the highest contribution at $\sqrt{s} = 1.5$ TeV and $\sqrt{s} = 3$ TeV.

[1] S. Chatrchyan *et al.* (CMS Collaboration), Phys. Lett. B **716**, 30 (2012).
[2] G. Aad *et al.* (ATLAS Collaboration), Phys. Lett. B **716**, 1 (2012).
[3] R. L. Delgado, A. Dobado, and F. J. Llanes-Estrada, J. Phys. G **41**, 025002 (2014).
[4] T. Appelquist and C. Bernard, Phys. Rev. D **22**, 200 (1980); A. Longhitano, Phys. Rev. D **22**, 1166 (1980); Nucl. Phys. **B188**, 118 (1981); A. Dobado, D. Espriu, and M. J. Herrero, Phys. Lett. B **255**, 405 (1991); B. Holdom and J. Terning, Phys. Lett. B **247**, 88 (1990); M. Golden and L. Randall, Nucl. Phys. **B361**, 3 (1991);
[5] F. Feruglio, Int. J. Mod. Phys. A **08**, 4937 (1993); L. M. Wang and Q. Wang, Chin. Phys. Lett. **25**, 1984 (2008); R. Alonso *et al.*, Phys. Lett. B **722**, 330 (2013); **726**, 926(E) (2013); G. Buchalla, O. Catà, and C. Krause, Nucl. Phys. **B880**, 552 (2014); **B913**, 475(E) (2016); C. Krause *et al.*, J. High Energy Phys. 05 (2019) 092.
[6] J. M. Cornwall, D. N. Levin, and G. Tiktopoulos, Phys. Rev. D **10**, 1145 (1974); C. E. Vayonakis, Lett. Nuovo Cimento **17**, 383 (1976); B. W. Lee, C. Quigg, and H. Thacker, Phys. Rev. D **16**, 1519 (1977); M. S. Chanowitz and M. K. Gaillard, Nucl. Phys. **261**, 379 (1985); P. B. Pal, arXiv:hep-ph/9405362.
[7] R. Delgado López, *Study of the Electroweak Symmetry Breaking Sector for the LHC* (Springer, Cham, 2017), https://inspirehep.net/literature/1611631.
[8] I. Asiáin, D. Espriu, and F. Mescia, Phys. Rev. D **105**, 015009 (2022).
[9] A. Dobado, C. Quezada-Calonge, and J. J. Sanz-Cillero, Nucl. Part. Phys. Proc. **312**, 191 (2021).
[10] P. A. Zyla *et al.* (Particle Data Group), Prog. Theor. Exp. Phys. **2020**, 083C01 (2020).
[11] C. Quezada-Calonge, A. Dobado, and J. J. Sanz-Cillero (to be published).
[12] A. Castillo, R. L. Delgado, A. Dobado, and F. J. Llanes-Estrada, Eur. Phys. J. C **77**, 436 (2017).
[13] M. J. Herrero and R. A. Morales, Phys. Rev. D **104**, 075013 (2021).
[14] A. Dobado, C. Quezada-Calonge, and J. J. Sanz-Cillero, Proc. Sci. ICHEP2020 (**2021**) 076.
[15] D. de Florian *et al.* (LHC Higgs Cross Section Working Group), *Handbook of LHC Higgs Cross Sections: 4. Deciphering the Nature of the Higgs Sector* (CERN, Geneva, 2017), https://inspirehep.net/literature/1494411.
[16] A. Pich, Les Houches Lect. Notes **108**, 137 (2020).
[17] M. J. Herrero and E. Ruiz Morales, Nucl. Phys. **B418**, 431 (1994).
[18] A. Pich, I. Rosell, J. Santos, and J. J. Sanz-Cillero, J. High Energy Phys. 04 (2017) 012.
[19] G. Buchalla and O. Cata, J. High Energy Phys. 07 (2012) 101.
[20] A. Dobado, A. Gomez-Nicola, A. L. Maroto, and J. R. Pelaez, *Effective Lagrangians for the Standard Model* (Springer, New York, 1997), 10.1007/978-3-642-59191-4.
[21] S. Dawson and G. Valencia, Nucl. Phys. **B348**, 23 (1991).
[22] D. Espriu and J. Matias, Phys. Rev. D **52**, 6530 (1995).
[23] P. B. Pal, arXiv:hep-ph/9405362.
[24] C. Grosse-Knetter and I. Kuss, Z. Phys. C **66**, 95 (1995).
[25] M. Jacob and G. C. Wick, Ann. Phys. (N.Y.) **7**, 404 (1959).
[26] T. Bahnik, arXiv:hep-ph/9710265.
[27] E. Arganda, C. Garcia-Garcia, and M. J. Herrero, Nucl. Phys. **B945**, 114687 (2019).
[28] J. de Blas, O. Eberhardt, and C. Krause, J. High Energy Phys. 07 (2018) 048.
[29] G. Aad *et al.* (ATLAS Collaboration), J. High Energy Phys. 07 (2020) 108; 01 (2021) 145(E); 05 (2021) 207(E).
[30] G. Aad *et al.* (ATLAS Collaboration), J. High Energy Phys. 07 (2020) 108; 01 (2021) 145(E).
[31] K. Agashe, R. Contino, and A. Pomarol, Nucl. Phys. **B719**, 165 (2005).

[32] S. Kanemura, K. Kaneta, N. Machida, and T. Shindou, Phys. Rev. D **91**, 115016 (2015).
[33] A. Denner and T. Hahn, Nucl. Phys. **B525**, 27 (1998).
[34] A. Dobado and D. Espriu, Prog. Part. Nucl. Phys. **115**, 103813 (2020).
[35] Thomas Hahn, Comput. Phys. Commun. **140**, 418 (2001).
[36] V. Shtabovenko, R. Mertig, and F. Orellana, Comput. Phys. Commun. **207**, 432 (2016).
[37] A. Denner, S. Dittmaier, and T. Hahn, Phys. Rev. D **56**, 117 (1997).
[38] A. Denner, S. Dittmaier, and R. Schuster, Nucl. Phys. **B452**, 80 (1995).
[39] K. J. Kallianpur, Phys. Lett. B **215**, 392 (1988).